Elsevier Editorial System(tm) for Applied Catalysis B: Environmental

Manuscript Draft

Manuscript Number: APCATB-D-16-00050R1

Title: Efficient WO3 Photoanodes Fabricated by Pulsed Laser Deposition for Photoelectrochemical Water Splitting with high Faradaic efficiency.

Article Type: Research Paper

Keywords: Pulsed Laser Deposition; WO3; water splitting; energy conversion; solar hydrogen

Corresponding Author: Dr. Cristian Fàbrega, Doctor

Corresponding Author's Institution: Universitat of Barcelona

First Author: Cristian Fàbrega, Doctor

Order of Authors: Cristian Fàbrega, Doctor; Sebastian Murcia-López, PhD; Damian Monllor-Satoca, PhD; Joan Daniel Prades, PhD; Maria Dolores Hernandez-Alonso, PhD; German Penelas; Joan Ramon Morante, Profesor; Teresa Andreu, PhD

Efficient WO_3 Photoanodes Fabricated by Pulsed Laser Deposition for Photoelectrochemical Water Splitting with high Faradaic efficiency.

C. Fàbrega[1,2,*], S. Murcia-López[1], D. Monllor-Satoca[1], J.D. Prades[2], M. D. Hernández-Alonso[3], G. Penelas[3], J.R. Morante[1,2], T. Andreu[1].

[1] Department of Advanced Materials for Energy, Catalonia Institute for Energy Research (IREC), Jardins de les Dones de Negre, 1, 08930 Sant Adrià de Besòs, Catalonia, Spain.
[2] Department of Electronics, Universitat de Barcelona (UB), Martí i Franquès, 1, 08028 Barcelona, Catalonia, Spain.
[3] Repsol Technology Center, Carretera de Extremadura A-5, km 18, 28935 Móstoles, Madrid, Spain.

[*]Corresponding author: Telf: +34934034804. E-mail: cfabrega@el.ub.edu (C. Fàbrega).

Abstract

In this work, we present a systematic study on the synthesis of monoclinic γ - WO_3 obtained using pulsed laser deposition (PLD). A photocurrent of 2.4 mA/cm^2 (60% of the optical maximum for a 2.7 eV gap material) was obtained for films as thick as 18 μm. FE-SEM images revealed that WO_3 films were actually formed by an array of oriented columns. Efficient hole extraction towards the electrolyte was observed and attributed to a possible accommodation of the electrolyte between the WO_3 columns, even for relatively compact films. This feature, combined with the detailed optical absorption and IPCE characterization, allowed us to implement a double-stack configuration of WO_3 photoanodes which resulted in a remarkable photocurrent density of 3.1 mA·cm^{-2} with 1 sun AM1.5G illumination in 0.1 M H_2SO_4 electrolyte. Faradaic efficiencies of more than 50% was obtained without co-catalyst, which is one the highest values reported for pure WO_3. By adding a 3 nm layer of Al_2O_3 by ALD, a faradaic efficiency of 80% was reached without diminishing the photocurrent density.

Keywords: Pulsed Laser Deposition; WO_3; water splitting; energy conversion; hydrogen production.

Manuscript

1. Introduction.

Photoelectrochemical (PEC) water splitting is still considered in contention for the most reliable technology for implementing the so-called solar-to-fuel economy [1]. Numerous efforts have been addressed to achieve a stable water photoelectrolysis system with materials able to absorb and convert the maximum amount of solar light. Among the materials of interest, metal oxides have centered most of the attention due to their inherent stability against photocorrosion, low cost, relative abundance, feasible scale up and mass production of PEC systems.

However, most of the traditional materials (i.e. TiO_2, Fe_2O_3 etc) are limited by their wide band gap [2,3] (TiO_2), poor electrical properties due to the very short hole life time [4] (Fe_2O_3) or improper band edge alignment for water splitting[1] (Fe_2O_3). Among them, WO_3 is recognized as one of the best positioned materials thanks to the wide range of synthetic process available [5–7] and the significant photon-to-current conversion efficiencies reported to date [8] for water oxidation. Other more complex materials like binary or ternary metal oxides, such as $BiVO_4$ [9–11], have emerged giving a new boost in the research of more efficient PEC systems. Similarly to Fe_2O_3, $BiVO_4$ [12] has deficient electrical properties and consequently, only thin films of tens of nanometers allow obtaining an efficient charge separation, resulting in a low solar light harvesting, limiting the overall performance. To overcome these constraints, some authors [13,14] opted by a different approach, implementing a host scaffold, or guest absorber, using WO_3. On top, thin films of $BiVO_4$ were deposited for an efficient charge separation at the interface of both materials and electron transport through the host material. For this reason, the development of these traditional materials is still of huge interest in spite of not fulfilling all the requirements for efficient PEC activity by themselves.

Another important aspect to consider, which is usually disregarded, is the reliability of the synthetic process in a large-scale scenario. Most synthetic processes are complex [12], involve

several steps [10] and their up scaling into large areas is not straightforward. This issue becomes much more evident in PEC devices made of different materials (e.g. host material, active material, blocking layers, catalyst, etc.), each one produced with different techniques [15].

Herein, we report on the synthesis of oriented and highly crystalline tungsten trioxide (WO_3) grown by Pulsed Laser Deposition (PLD) using preindustrial equipment able to process up to 4-inch-substrates with high uniformity and reproducibility. A complete and systematic study on the PLD growth parameters (e.g. oxygen pressure, temperature, number of pulses, etc.) allowed us to achieve one of the highest photocurrents densities in a water splitting system under simulated sunlight with pure WO_3 photoanodes, with an unprecedented synthesis ease and potential for scaling up. From the optical characteristics, IPCE and the film thickness optimization, we quantified some fundamental semiconductor features such as electrical transport properties, depletion region width and optical absorption coefficients (α). Additionally, a stack of two photoanodes is presented as a promising configuration to overcome the dichotomy between charge carrier collection and light absorption, typical in most metal oxide photoelectrodes. Finally, to improve the faradaic efficiency of our photoanodes two different strategies have been followed: alumina ALD coating and IrO_2 deposition.

2. Materials and methods.

2.1 Films deposition and OEC

Fluorine-doped tin oxide (FTO) glass substrates of 2 cm x 1.5 cm were used. Before deposition, glass pieces were cleaned with a subsequent sonication in acetone, isopropanol and double deionized water followed by a drying process with N_2 stream. WO_3 films were deposited by pulsed laser deposition (PLD) in a PLD 5000 equipment (PVD products Inc.) with a 240 nm excimer KrF laser. Substrates were placed facing down over a stainless steel shadow mask with a 1 cm x 1 cm square window. A commercial target (American Elements Inc.) was used as WO_3 source. The distance between the target and the substrate was kept at 90 mm for all depositions, and the frequency of the laser set at 10 Hz. Temperature, laser energy, number of pulses and oxygen pressure inside the chamber were used as control parameters to optimize for the PLD deposition. Samples names have been labeled PLD-X, where X is the approximate thickness of the sample in micrometers.

Alumina conformal coating were deposited by means of an Atomic Layer Deposition equipment from Cambridge NanoTech (Savannah). Trimethylaluminum (TMA) was used as aluminum source during the ALD process and water as an oxidizing agent. Growth temperature was fixed at 200◦C with a sequence of 2 ms of TMA followed by 2 ms of water. A total of 33 cycles were applied to obtain 3 nm of Al_2O_3, corresponding to a growth rate of 0.9 Å/cycle.

IrO_x deposition on the WO_3 electrode was performed by drop-casting. For this purpose, an IrO_x colloid was previously obtained by following the recipe reported in literature[16]. Firstly, 0.008 g of K_2IrCl_6 (Technical grade, Sigma-Aldrich) was added to 100 mL of Milli-Q water. Then, the necessary amount of a 0.5M NaOH solution was added until reaching a pH value of 12. After this, the mixture was heated at 80ºC until complete dissolution of the K_2IrCl_6. In a second step, this solution was cooled with an ice-bath at 5ºC and the pH value was adjusted again with a

0.5M HNO_3 solution to 8. Finally, the solution was heated at 80ºC for 30 min and a bluish IrO_2 colloid was obtained.

2.2 Characterization and Photoelectrochemical Measurements

The crystalline phase composition of the PLD products was determined by X-ray diffraction (XRD) measurements in a Bruker D8 Advance diffractometer equipped with a Cu Kα (1.54051 Å) radiation source, a LYNXEYE super speed detector, Bragg-Brentano configuration and a Ni filter. Optical characterization was performed in a Lambda 950 UV-Vis-NIR Spectrometer (PerkinElmer) equipped with a 150 mm Integrating Sphere and Spectralon standard. Transmittance and Reflectance measurements were separately carried out for each sample in a wavelength range of 300-800 nm, with a step of 5 nm. The morphology of the as-prepared samples was observed by field-emission scanning electron microscopy (FE-SEM, Zeiss Auriga). Thicknesses of the samples were measured by profilometry with a KLA-Tencor P15 equipment with a low force head. 3D images were obtained with a Sensofar non-contact optical 3D confocal interferometer. Photoelectrochemical (PEC) measurements were conducted in a three-electrode quartz cell connected to a Parstat 2273 potentiostat. A 0.1 M H_2SO_4 solution was used as electrolyte, a Pt mesh as counter electrode and Ag/AgCl (3 M) ($E^º$ = 0.203 V vs NHE) as reference electrode. The results are presented against the reversible hydrogen electrode (RHE), calculated from the Nernst equation. Cyclic voltammetries with a sweep rate of 40 $mV \cdot s^{-1}$ were recorded in the dark and under illumination with simulated AM1.5G solar light provided by a portable solar simulator (Peccell, PEC-L01).

The incident photon to current conversion efficiency (IPCE) was measured at a constant bias of 1.23 V vs RHE in a 0.1 M H_2SO_4 electrolyte using a wavelength range of 300 to 550 nm with an interval step of 5 nm and a stabilization time of 2 minutes between measurements, with a light on-off time cycle at each wavelength of 90 s and 30 s, respectively. Monochromatic illumination was supplied by a LS Xenon Light Source (ABET technologies) connected to an

Oriel Cornerstone 260 1/4m monochromator. Photon flux was estimated by calibrating the monochromatic light with a Silicon Photodiode (Thorlabs, S120VC).

The O_2 concentration in the anolyte was monitored with a fiber optical oxygen transmitter Fibox 3 trace V3 (PreSens). The device is equipped with two sensors: a sensor coating type PSt3 (detection limit 15 ppb) and a temperature sensor for compensation during the tests. Previous degasification of the three-electrode cell (without head space) with N_2 flow was performed, after which the electrodes were illuminated (AM1.5 G, 1 Sun) during 30 min at 1.23V vs RHE. The baseline drift in the O_2 concentration was estimated immediately before and after the (photo)electrolysis and was compensated in each experiment by linear extrapolation.

3. Results and discussion.

Among all polymorphs, γ-WO_3 monoclinic is the most stable and photoactive phase. This crystal structure is very sensitive to both temperature and defects, i.e. oxygen vacancies [17]. A preliminary study on the effect of substrate temperature and oxygen partial pressure in the PLD chamber was performed in order to determine the optimal deposition parameters. Photoelectrochemical measurements showed that 400ºC and 100 mTorr of partial oxygen pressure provided the best performing samples (S1). All films deposited in a temperature range from 300 to 600ºC and oxygen partial pressure from 50 to 200 mTorr presented monoclinic structure (S2). At lower oxygen pressures, the layers were highly reduced looking black colored and displaying almost no photoactivity.

WO_3 film thickness was optimized by fixing substrate temperature and oxygen pressure at 400ºC and 100 mTorr respectively, while increasing the number of pulses and/or the nominal energy of the laser between 300 and 550 mJ. It was found that only the deposition rate was affected by the laser energy. A perfect correlation between thickness and the total amount of energy (i.e. product of number of pulses and laser energy) with a rate of 5400 mJ per nanometer was determined (S3). Samples with thicknesses ranging from 573 nm to more than

17 μm were fabricated (Table I). A 3D reconstruction with the confocal microscope showed uniform thicknesses through the entire 1 cm x 1 cm samples (S4).

Field Emission Scanning Electron Microscopy images (Figure 1) showed that the surface of WO_3 grown by PLD was uniform and finished with a pyramidal-like pattern. A detailed view of a SEM cross section revealed that in fact, these WO_3 films consisted of an array of oriented compact columns (Figure 1). This apparent orientation was confirmed by XRD analysis (Figure 2). As WO_3 thickness increased, all reflections except the (002) of the monoclinic phase started to disappear, which implies the predominance of this orientation.

Figure 3 shows the photocurrent density versus potential curves for all WO_3 films with different thicknesses, measured in 0.1 M H_2SO_4 electrolyte under AM 1.5G irradiation (100 mW cm^{-2}) from both front (EE) and back (SE) illumination. Open circuit voltages were in all cases around 0.5 V vs RHE and current densities increased with increasing WO_3 thickness, reaching a photocurrent density of 2.4 $mA \cdot cm^{-2}$ at 1.23 V vs RHE for the thickest sample (17.6 μm), which is one of the highest photocurrent densities for WO_3 photoanodes reported to date [5,17,18]. Bearing in mind that optically WO_3 could achieve a maximum of 4.0 $mA \cdot cm^{-2}$ (2.7 eV bandgap) [19], this represents a 60% of the optical maximum, that has been achieved in the absence of additional structural (i.e. doping) or surface modifications (e.g. plasmonic nanoparticles, heterojunctions, passivation, etc).

To gain further insight into the mechanistic aspects of the charge transfer phenomena, the IPCE of all samples (Figure 4) were recorded at 1.23V vs RHE under EE and SE illumination. A summary of the photocurrent densities, calculated by convoluting the IPCE with the AM 1.5G solar irradiation spectra (S5), can be found in Table I. The first thing to note from the IPCE spectra (Figure 4) is the notorious decrease in the region between 300 and 340 nm when illuminating from the back side due to the absorption of light by the FTO layer. At the same time, huge improvements in the IPCE values at long wavelengths (390-480 nm) were found

due to the increased absorption capability of thicker WO_3 films, as shown in the UV-vis spectra (S6). To determine the absorption coefficient, we deposited a WO_3 layer over a quartz substrate in order to avoid the FTO absorption. From the transmittance and reflectance spectra, the absorption coefficient was inferred. Along with the absorption coefficient spectrum, we plotted the corresponding penetration length, considering 63%, 83% and 95% of the absorbed light (Figure 5a). The absorption coefficient cannot be properly estimated in the region of short and long wavelengths and, for that reason, we restrained the experimental fitting to the 380-440 nm range.

It is clear that the absorption coefficient of WO_3 is quite low compared to other materials (e.g. 10^5 to 10^6 cm^{-1} for hematite [20]) , which implies that thicker films are needed if fully absorption of the solar spectrum above the band gap is required. For example, for a wavelength close to the band gap of WO_3 (460 nm), a 4 μm thick layer is needed to absorb 63% of this light; and a 12 μm thick one to absorb 95%. The absorption profile is remarkably coincident with the IPCE values obtained for increasing thicknesses of WO_3 films (figure 5b): the maximum value of the IPCE at each wavelength is reached, in both EE and SE illumination, when WO_3 film thickness is above the penetration depth corresponding to 95% absorption. Remarkably, IPCE values of up to 70% are reached, in line with mesoporous WO_3 thick films with randomly oriented nanoparticles [17].

Of course, light absorption is not the only important parameter to be taken into account in order to obtain top performance photoanodes. Separation and transport of the photogenerated charge carriers must be considered. For example, considering that upon front illumination shorter wavelengths are absorbed within the first 2 μm, in case of thicker samples, electrons must still flow along several μm to reach the FTO back contact, which implies that electron transport is dominated by diffusion in a similar fashion to the Södergren model for microporous semiconductors [21]. Thus, an estimated minimum apparent diffusion length of

15 μm can be inferred. These values of electron diffusion lengths [22] are in the same order of magnitude that of the ones obtained for TiO_2 in dye sensitized solar cells [23], which generally have values that could even exceed the electrode thickness. Assuming that this is the case of our films [17], from the Södergren model it can be inferred that the diffusion length is 2 to 3 times larger than the electrode thickness (S7). Accordingly, a lower (bulk) recombination rate for both thin and thick films could be invoked to justify such large diffusion lengths [24]. However, in the case of back illumination, at short wavelengths (300 - 380 nm) electrons can also be generated in abundance close to the FTO contact and holes must travel long distances. Hole diffusion at micron distances is highly unlikely (diffusion length L_p in WO_3 is around 400 nm [25]). A possible explanation to the high photocurrent observed with back illumination (and thus a high hole collection in the electrolyte) involves the structure of the WO_3 layers: the column-like structure can be penetrated by the electrolyte leading to shorter distances between the hole generation sites (inside the WO_3 columns) and the hole collector (electrolyte). In this way, holes can be efficiently separated and transferred to the electrolyte (which would be at reach right after photo generation), while electrons can diffuse inside WO_3 columns for longer distances.

To prove that the electrolyte effectively penetrates into the WO_3 layers, the amount of accumulated/extracted charge was determined by integrating dark voltammetries for each thickness (S8). The capacitive behavior of a voltammetry in the dark relates to the insertion-deinsertion of cations in charge accumulation (i.e. negative polarization). As the cation insertion occurs at the electrolyte/electrode interface, the charge can be directly correlated to the electrochemically active surface area of the material. In compact flat films, total charge values should be less dependent of the film thickness. In the present case, the total charge increases with the film thickness (S8), which implies that a larger WO_3 surface is in contact with the electrolyte for thicker samples.

In this regard, it is interesting that considering the IPCE values at a given wavelength for different sample thicknesses, one may observe that at shorter wavelengths the increment of the IPCE values is very strong, up to almost 2 μm thick samples (Figure 5b). A similar trend can be observed in the plot of the photocurrent density as a function of the WO_3 film thickness (Figure 6). These two different regimes (a steep increase up to 2 μm and a slower one from there on) can be explained taking into account the extension of the surface depleted region. It is well known that the depletion region in a semiconductor is the key factor for efficient charge carrier separation [26]. In a first approximation, the Poisson equation can be analytically solved for planar, cylindrical and spherical structures [27]. For each structure (i.e. in 1D, 2D and 3D respectively) there is a characteristic dimension, or a geometrical parameter (R_0), that rules the dependence of the potential drop within the depletion region. These R_0 parameters are the thickness, for planar structures, and the radius for the cylindrical and spherical ones. In all cases, one can distinguish two different regimes: (I) when the depletion region (W) is shorter than the characteristic dimension (R_0) or (II) when it is longer [27]:

$$\theta \propto {R_0}^2 \qquad \text{for } W \leq R_0 \qquad (1)$$

$$\theta \propto W^2 \sim ct. \qquad \text{for } W > R_0 \qquad (2)$$

where θ is a dimensionless variable that is related to the potential drop at the semiconductor surface (measured with respect to the center of the semiconductor) given by $\theta = e\phi_{SC}/kT$, where k is the Boltzmann constant (1.38×10^{-23} J·K^{-1}), ϕ_{SC} is the potential in the space charge region (E - E_{fb}, where E_{fb} is the flat-band potential) and T is the absolute temperature in K. From these expressions, it is clear that when W < R_0 the potential increases quadratically with the radius. Thus, the electron-hole separation capability and the resulting photocurrent increase rapidly as well. In contrast, when W > R_0 the potential drop remains steady in a

maximum value (corresponding to the value at W = R_0), which is independent on the geometrical parameter.

In our case, the PEC layer was made of independent WO_3 nanorods with a depleted shell. Therefore, the geometrical parameter is the diameter of the nanorods formed during the PLD process. When increasing the number of PLD pulses, not only the nanorods get longer, but also their diameter increases. Consequently, the first regime corresponds to thinner films (i.e. thinner nanorods) in which the voltage drop inside the depletion region can increase steeply, dominated by the quadratic relationship with the radius (Eq. 1), up to a maximum value. When the potential drop is maximum, i.e. the diameter of the nanorod is enough to develop completely the electric field related to the depletion region, charge separation is not further improved. From then on, IPCE and photocurrent density increase more slowly, only affected by the increase in the amount of the absorbed light or the exposed surface area to the electrolyte. Indeed, if we correlate the photocurrent values with the relative charge of the electrodes (as a measure of the surface area from dark voltammetry), we observe a similar correlation to that of the depletion layer width, pointing out that the surface area is also crucial in determining the final photoactivity yield of the electrodes (S9).

In order to tackle the optimizacion of light absorption by the material, a stack of PLD-11.5 and PLD-17.6 samples was built (keeping the WO_3 layers in the outer side, as shown in the inset in Fig. 7a) seeking the full absorption of the solar light by WO_3 layer while preserving the good charge extraction properties observed in these samples separately. *j-E* curves of Figure 7a show that the stacking of both samples resulted in a maximum photocurrent density of 3.1 $mA \cdot cm^{-2}$ (78% of the optical maximum for WO_3), which means an increase of almost 30% with respect to PLD-11.5 and PLD-17.6, separately. According to the characterization of the individual WO_3 photoanodes, it is likely that longer wavelengths were partially transmitted through the first WO_3 film and reabsorbed by the second one. Although only a small

percentage of these long wavelengths were transmitted, their contribution to the total photocurrent can be very important considering that the irradiance at longer wavelengths is greater than at shorter wavelengths. Figure 7b presents the relative increment of the spectral response (IPCE) of each component (PLD -11.5 and PLD – 17.6) with respect to the measured IPCE of the double-stacked sample. Comparing the results of the stack with sample PLD–17.6 EE, an increment of up to 50% was achieved in the range from 440 nm to 475 nm and only 3% in the remaining range. In contrast, the ratio between PLD – 11.5 SE and the stacked configuration showed a decrease from 440 nm onwards, indicating that PLD – 11.5 SE is the main responsible of the absorption of light at long wavelengths. The increase at short wavelengths is only due to the absorption of light by the FTO/glass substrates when illuminated from the back. For this reason, the spectrum was truncated below 360 nm.

This stacking approach is especially attractive for semiconductors where electron and hole transport properties are a limiting factor in thick films, as shown by Itoh et al. for thin hematite films [28]. For example, it is well known that Fe_2O_3 [29] and $BiVO_4$ [25] display poor electrical properties and high recombination rates. Film thickness around 40-150 nm (or even less in the case of Fe_2O_3) are typical values for the best performing photoanodes [30,31]. As light penetration depth in these materials is as long as 500 nm for longer wavelengths, most of the light is transmitted and lost. Thus, double side configurations as the one proposed in this work offer a straight forward path to enhance the light collection capabilities, without worsening the transport properties. As such, with the transport and light absorption hassles solved, the photoanode optimization lies in the surface reactivity and the hole transfer efficiency to the species at the interface of the electrolyte.

Finally, in order to determine the faradaic efficiency of the oxygen evolution reaction (OER), the O_2 concentration was measured with an optical O_2 sensor. To that end, several WO_3 samples with around 1.7 μm thickness were fabricated. It is well known that, in general, wide

band gap semiconductors might reduce the counter-anions present in the electrolyte rather than reduce water to produce oxygen [32,33]. Particularly, WO_3 has shown faradaic efficiencies of around 30% or less due to the formation of peroxo species and/or reduction of counter anions [6,34] . Several strategies have been followed with the aim of improving the OER faradaic efficiency. Kim et al.[6] demonstrated that an alumina coating of only few nanometers is enough to hamper most of the competing reactions, yielding a faradaic efficiency of 50%. In line with that work, a 3 nm ALD coating of alumina was applied on one of the PLD WO_3 samples fabricated for this purpose. Notably, the photoactivity was slightly improved by the ALD deposition (S10). In our case, the bare WO_3 sample showed a 50% of faradic efficient (Figure 8), which is already much higher than the faradaic efficiency reported elsewhere with bare WO_3. However, by introducing a 3 nm ALD layer of Al_2O_3 on top of the WO_3, the faradaic efficiency reached almost 80% (Figure 8a). This outstanding result is of tremendous relevance, as usually, expensive and scarce materials, such as Iridium, are needed to obtain acceptable values of faradaic efficiency for the oxygen evolution reaction in acid electrolyte.

To further evaluate the reliability of the Al_2O_3 as a catalyst for the oxygen evolution reaction, a 3 nm layer were deposited on top of the thickest WO_3 sample (PLD – 17.6). Although a faradaic efficiency of 60% was achieved with this procedure (Figure 8b), which supposed an increase respect to the bare sample (FF = 45%), the numbers obtained with thinner samples were considerably higher (65-80%). Furthermore, the photocurrent density was slightly hampered by the presence of the alumina layer, decreasing form the original 2.4 $mA \cdot cm^{-2}$ to 2.1 $mA \cdot cm^{-2}$. A plausible explanation, in the absence of further study, is that the deposition conditions of the ALD alumina layer must be adapted for an efficient conformal coverage in samples with very high aspect ratios and very small porous, as is the case of the PLD – 17.6 compared with the previous samples with only 1.7 μm thickness.

4. Conclusions.

Monoclinic γ-WO_3 films were successfully deposited on FTO substrates by pulsed laser deposition. These films showed a columnar-shape structure, which resulted to be crucial in the photoanodes performances as the electrolyte was able to penetrate within the columns contributing to improve the charge transport. As the electrolyte was in contact with the walls of the WO_3 columns, holes path lengths were low enough for an efficient injection into the electrolyte. On the other hand, it has been demonstrated that electrons, with much longer diffusion lengths, were able to travel the whole electrode thickness to reach the FTO back contact. Both efficient hole injection into the electrolyte and long electron diffusion lengths were essential because of the low absorption coefficient of WO_3. By virtue of their morphology, thick films fabrication were attainable in order to collect and absorb the maximum amount of solar light, obtaining remarkably high photocurrent densities, up to 2.4 $mA \cdot cm^{-2}$ (60% of the optical maximum). Furthermore, to ensure a full absorption of the light, a new configuration has been presented in the form of two stacked WO_3 samples. In this configuration, 3.1 $mA \cdot cm^{-2}$ were obtained (78% of the optical maximum), which is one of the highest photocurrent densities reported for unmodified WO_3 photoanodes. Likewise, a faradaic efficiency of more than 50% was obtained without co-catalyst WO_3.

By adding a 3 nm layer of Al_2O_3 by ALD, a faradaic efficiency of 80% was reached without diminishing the photocurrent density. However, for thicker samples, both faradaic efficiency and photocurrent density were hampered by the presence of the alumina layer. A further study is necessary in order to determine the proper deposition conditions to obtain the same performances for thicker samples.

PLD proved to be a suitable technique for the deposition of metal oxide films on large areas, even those with a much more complex stoichiometry thanks to the perfect transfer from target to substrate.

5. Acknowledgements

This work was supported by Repsol, S.A. IREC also acknowledges additional support by the European Regional Development Funds (ERDF, FEDER Programa Competitivitat de Catalunya 2007-2013), by MINECO project ENE2012-3651, MAT2014-59961-C2-1-R and Multicat (CSD2009- 00055), and the Framework 7 program projects SOLAROGENIX (FP7-NMP-2012-310333) and CEOPS (FP7-NMP-2012-309984). J.D. Prades acknowledges the support from the Serra Húnter Programme.

Figure Caption

Figure 1 Top view and cross section FE-SEM images showing the characteristic pyramidal-like shape and the columnar orientation of a WO_3 PLD deposited on an FTO substrate.

Figure 2 XRD spectra for all samples with increasing thickness. Two reflections of WO_3 monoclinic phase are indexed, (020) and (022), showing that a preferential growth through (020) crystallographic planes is obtained in our PLD deposited samples.

Figure 3 Photocurrent density obtained under 100 $mW \cdot cm^{-2}$ simulated sunlight from both, **(a)** front (EE) and **(b)** back (SE) illumination. All measurements were recorded at a scan rate of 40 $mV \cdot s^{-1}$ using an Ag/AgCl reference electrode in a 0.1M H_2SO_4 electrolyte. Potential have been referred to the reversible hydrogen electrode (RHE). Measured dark currents of all samples were below 50 $\mu A \cdot cm^{-2}$ (not plotted).

Figure 4 (a) Front (EE) and **(b)** back (SE) illumination IPCE spectra recorded at 1.23 V vs RHE in a 0.1 M H_2SO_4 electrolyte using a wavelength range of 300 to 550 nm with an interval step of 5 nm and a stabilization time of 2 minutes between measurements (light on, 90 s; light off, 30 s).

Figure 5 (a) Absorption coefficient calculated from the UV-vis spectra and the corresponding penetration depth considering 63% ($1/\alpha$), 83% ($2/\alpha$) and 95% ($3/\alpha$) of absorbed light. Dashed lines correspond to fittings made in the intermediate region of the spectrum (380-440 nm) because the experimental data in high and low absorption regions were not accurate. **(b)** IPCE as a function of WO_3 film thickness at different wavelengths (410, 430, 450 and 470 nm) with front (EE) and back (SE) illumination.

Figure 6 Photocurrent density as a function of WO_3 thickness. Two regions with different trends are highlighted showing the transition between an almost fully depleted films with a lower potential drop ($W > R_0$) and the classical potential drop expression in a semiconductor ($W < R_0$).

Figure 7 (a) Photocurrent density under 100 $mW \cdot cm^{-2}$ simulated sunlight of a double stacked configuration compared with the corresponding individual WO_3 photoelectrodes (PLD – 17.6 EE and PLD – 11.5 SE). All measurements were recorded at a scan rate of 40 $mV \cdot s^{-1}$ using an Ag/AgCl reference electrode in a 0.1M H_2SO_4 electrolyte. Potential have been referred to the reversible hydrogen electrode (RHE). Measured dark currents of all samples were below 50 $\mu A \cdot cm^{-2}$ (not plotted). **(b)** IPCE of PLD-11.5 and PLD–17.6 and the corresponding stacked configuration. (Inset) Relative IPCE increment of PLD-11.5 and PLD–17.6 with respect to the stacked configuration as a function of wavelength. The spectra have been truncated at 360 nm because the relative IPCE between the stack and PLD–11.5 SE is strongly affected by the absorption of light through the FTO/glass substrate.

Figure 8 (a) Oxygen evolution reaction faradaic efficiency of a bare WO_3 sample, an ALD coated sample with 3 nm of alumina. **(b)** *j*-E curve and the corresponding faradaic efficiency of PLD – 17.6 sample with and without alumina co-catalyst.

Table I. Summary of electrode thicknesses and photocurrents for all prepared films

Sample	Thickness* ±10 (nm)	J_{ph}(EE)** ±0.01 (mA·cm^{-2})	J_{ph}(SE)** ±0.01 (mA·cm^{-2})	EE-IPCE @350 nm ±0.1 (%)	EE-IPCE @450 nm ±0.1 (%)	SE-IPCE @350 nm ±0.1 (%)	SE-IPCE @450 nm ±0.1 (%)
PLD – 0.5	*570*	*1.07*	*1.01*	*64.8*	*1.7*	*50.4*	*1.9*
PLD – 0.8	*840*	*1.26*	*1.35*	*65.0*	*2.9*	*55.6*	*3.3*
PLD – 1.0	*1030*	*1.40*	*1.47*	*65.3*	*4.2*	*50.7*	*4.7*
PLD – 1.7	*1700*	*1.61*	*1.60*	*59.7*	*5.9*	*46.9*	*7.0*
PLD – 3.4	*3420*	*1.71*	*1.91*	*54.9*	*13.2*	*48.1*	*12.9*
PLD – 8.1	*8100*	*2.03*	*2.02*	*55.9*	*23.0*	*35.9*	*25.5*
PLD – 11.5	*11500*	*2.26*	*2.20*	*55.1*	*30.1*	*35.6*	*31.6*
PLD – 17.6	*17600*	*2.40*	*2.35*	*40.3*	*27.2*	*36.5*	*29.5*

* Thickness was measured using a KLA-Tencor P15 profiler.

** Photocurrent density was measured from *j-E* curves at 1.23 V vs RHE with 1 sun AM1.5G illumination in 0.1 M H_2SO_4 electrolyte.

References

[1] Z. Li, W. Luo, M. Zhang, J. Feng, Z. Zou, Photoelectrochemical cells for solar hydrogen production: current state of promising photoelectrodes, methods to improve their properties, and outlook, Energy Environ. Sci. 6 (2013) 347–370.

[2] C. Fàbrega, T. Andreu, F. Güell, J.D. Prades, S. Estradé, J.M. Rebled, et al., Effectiveness of nitrogen incorporation to enhance the photoelectrochemical activity of nanostructured TiO_2:NH_3 versus H_2-N_2 annealing., Nanotechnology. 22 (2011) 235403.

[3] C. Fàbrega, T. Andreu, A. Tarancón, C. Flox, A. Morata, L. Calvo-Barrio, et al., Optimization of surface charge transfer processes on rutile TiO2 nanorods photoanodes for water splitting, Int. J. Hydrogen Energy. 38 (2013) 2979–2985.

[4] D. Monllor-Satoca, M. Bärtsch, C. Fàbrega, A. Genç, S. Reinhard, T. Andreu, et al., What do you do, titanium? Insight into the role of titanium oxide as a water oxidation promoter in hematite-based photoanodes, Energy Environ. Sci. (2015).

[5] J. Su, X. Feng, J.D. Sloppy, L. Guo, C.A. Grimes, Vertically Aligned WO_3 Nanowire Arrays Grown Directly on Transparent Conducting Oxide Coated Glass: Synthesis and Photoelectrochemical Properties, Nano Lett. 11 (2010) 203–208.

[6] W. Kim, T. Tachikawa, D. Monllor-Satoca, H. Kim, T. Majima, W. Choi, Promoting water photooxidation on transparent WO_3 thin films using an alumina overlayer, Energy Environ. Sci. 6 (n.d.) 3732–3739.

[7] C. Santato, M. Ulmann, J. Augustynski, Enhanced Visible Light Conversion Efficiency Using Nanocrystalline WO_3 Films, Adv. Mater. 13 (2001) 511–514.

[8] J. Brillet, J.-H. Yum, M. Cornuz, T. Hisatomi, R. Solarska, J. Augustynski, et al., Highly efficient water splitting by a dual-absorber tandem cell, Nat. Photonics. 6 (2012) 824–828.

[9] Y. Park, K.J. McDonald, K.-S. Choi, Progress in bismuth vanadate photoanodes for use in solar water oxidation, Chem. Soc. Rev. 42 (2013) 2321–2337.

[10] T.W. Kim, K.-S. Choi, Nanoporous $BiVO_4$ photoanodes with dual-layer oxygen evolution catalysts for solar water splitting, Science (80-.). 343 (2014) 990–994.

[11] F.F. Abdi, L. Han, A.H.M. Smets, M. Zeman, B. Dam, R. van de Krol, Efficient solar water splitting by enhanced charge separation in a bismuth vanadate-silicon tandem photoelectrode., Nat. Commun. 4 (2013) 2195.

[12] F.F. Abdi, T.J. Savenije, M.M. May, B. Dam, R. van de Krol, The Origin of Slow Carrier Transport in $BiVO_4$ Thin Film Photoanodes: A Time-Resolved Microwave Conductivity Study, J. Phys. Chem. Lett. 4 (2013) 2752–2757.

[13] K. Sivula, F. Le Formal, M. Grätzel, WO_3–Fe_2O_3 Photoanodes for Water Splitting: A Host Scaffold, Guest Absorber Approach, Chem. Mater. 21 (2009) 2862–2867.

[14] J. Su, L. Guo, N. Bao, C.A. Grimes, Nanostructured WO_3/$BiVO_4$ Heterojunction Films for Efficient Photoelectrochemical Water Splitting, Nano Lett. 11 (2011) 1928–1933.

[15] X. Shi, I.Y. Choi, K. Zhang, J. Kwon, D.Y. Kim, J.K. Lee, et al., Efficient photoelectrochemical hydrogen production from bismuth vanadate-decorated tungsten trioxide helix nanostructures, Nat. Commun. 5 (2014) 4775.

[16] Z. Wang, G. Liu, C. Ding, Z. Chen, F. Zhang, J. Shi, et al., Synergetic Effect of Conjugated $Ni(OH)_2$ /IrO_2 Cocatalyst on Titanium-Doped Hematite Photoanode for Solar Water Splitting, J. Phys. Chem. C. 119 (2015) 19607–19612.

[17] G. Wang, Y. Ling, H. Wang, X. Yang, C. Wang, J.Z. Zhang, et al., Hydrogen-treated WO_3 nanoflakes show enhanced photostability, Energy Environ. Sci. 5 (2012) 6180–6187.

[18] J. Zhang, P. Zhang, T. Wang, J. Gong, Monoclinic WO_3 nanomultilayers with preferentially exposed (002) facets for photoelectrochemical water splitting, Nano Energy. 11 (2015) 189–195.

[19] C. Liu, N.P. Dasgupta, P. Yang, Semiconductor Nanowires for Artificial Photosynthesis, Chem. Mater. 26 (2014) 415–422.

[20] J.H. Kennedy, Photooxidation of Water at α-Fe_2O_3 Electrodes, J. Electrochem. Soc. 125 (1978) 709.

[21] S. Soedergren, A. Hagfeldt, J. Olsson, S.-E. Lindquist, Theoretical Models for the Action Spectrum and the Current-Voltage Characteristics of Microporous Semiconductor Films in Photoelectrochemical Cells, J. Phys. Chem. 98 (1994) 5552–5556.

[22] H. Wang, J. He, A. Hagfeldt, S. Lindquist, Photolelectrochemistry of Nanostructured WO_3 Thin Film Electrodes for Water Oxidation : Mechanism of Electron Transport, J. Phys. Chem. B. 104 (2000) 5686–5696.

[23] J. Navas, E. Guillén, R. Alcántara, C. Fernández-Lorenzo, J. Martín-Calleja, G. Oskam, et al., Direct Estimation of the Electron Diffusion Length in Dye-Sensitized Solar Cells, J. Phys. Chem. Lett. 2 (2011) 1045–1050.

[24] D. Monllor-Satoca, L. Borja, A. Rodes, R. Gómez, P. Salvador, Photoelectrochemical behavior of nanostructured WO_3 thin-film electrodes: The oxidation of formic acid., Chemphyschem. 7 (2006) 2540–51.

[25] R.A. Pala, A.J. Leenheer, M. Lichterman, H.A. Atwater, N.S. Lewis, Measurement of minority-carrier diffusion lengths using wedge-shaped semiconductor photoelectrodes, Energy Environ. Sci. 7 (2014) 3424–3430.

[26] C. Fàbrega, D. Monllor-Satoca, S. Ampudia, A. Parra, T. Andreu, J.R. Morante, Tuning the fermi level and the kinetics of surface states of TiO_2 nanorods by means of ammonia treatments, J. Phys. Chem. C. 117 (2013) 20517–20524.

[27] E. Comini, V. Guidi, C. Malagù, G. Martinelli, Z. Pan, G. Sberveglieri, et al., Electrical Properties of Tin Dioxide Two-Dimensional Nanostructures, J. Phys. Chem. B. 108 (2004) 1882–1887.

[28] K. Itoh, Thin Film Photoelectrochemistry: Iron Oxide, J. Electrochem. Soc. 131 (1984) 1266.

[29] H. Dotan, O. Kfir, E. Sharlin, O. Blank, M. Gross, I. Dumchin, et al., Resonant light trapping in ultrathin films for water splitting., Nat. Mater. 12 (2013) 158–64.

[30] A. Kay, I. Cesar, M. Gratzel, New Benchmark for Water Photooxidation by Nanostructured α-Fe_2O_3 Films, J. Am. Chem. Soc. 128 (2006) 15714–15721.

[31] Y. Qiu, S.-F. Leung, Q. Zhang, B. Hua, Q. Lin, Z. Wei, et al., Efficient photoelectrochemical water splitting with ultrathin films of hematite on three-dimensional nanophotonic structures., Nano Lett. 14 (2014) 2123–9.

[32] J.M. Spurgeon, J.M. Velazquez, M.T. McDowell, Improving O_2 production of WO_3 photoanodes with IrO_2 in acidic aqueous electrolyte., Phys. Chem. Chem. Phys. 16 (2014) 3623–31.

[33] C.R. Lhermitte, J. Garret Verwer, B.M. Bartlett, Improving the stability and selectivity for the oxygen-evolution reaction on semiconducting WO_3 photoelectrodes with a solid-state FeOOH catalyst, J. Mater. Chem. A. (2016).

[34] Q. Mi, A. Zhanaidarova, B.S. Brunschwig, H.B. Gray, N.S. Lewis, A quantitative assessment of the competition between water and anion oxidation at WO_3 photoanodes in acidic aqueous electrolytes, Energy Environ. Sci. 5 (2012) 5694.

Figure 1

Click here to download high resolution image

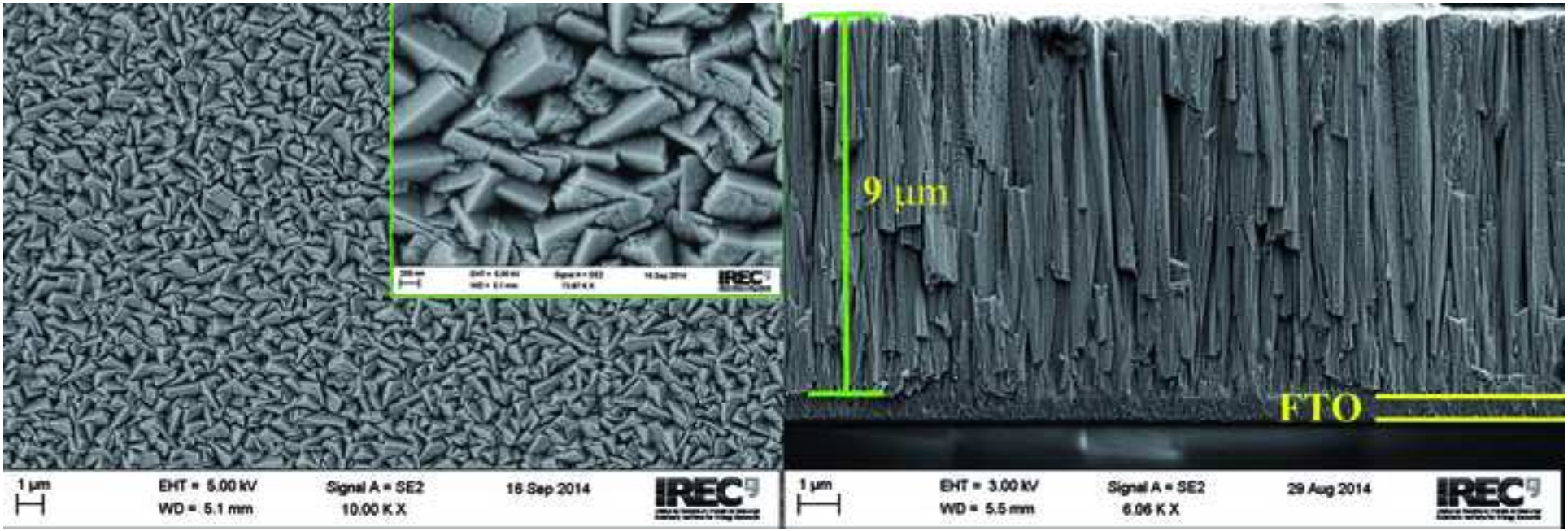

Figure 2

Click here to download high resolution image

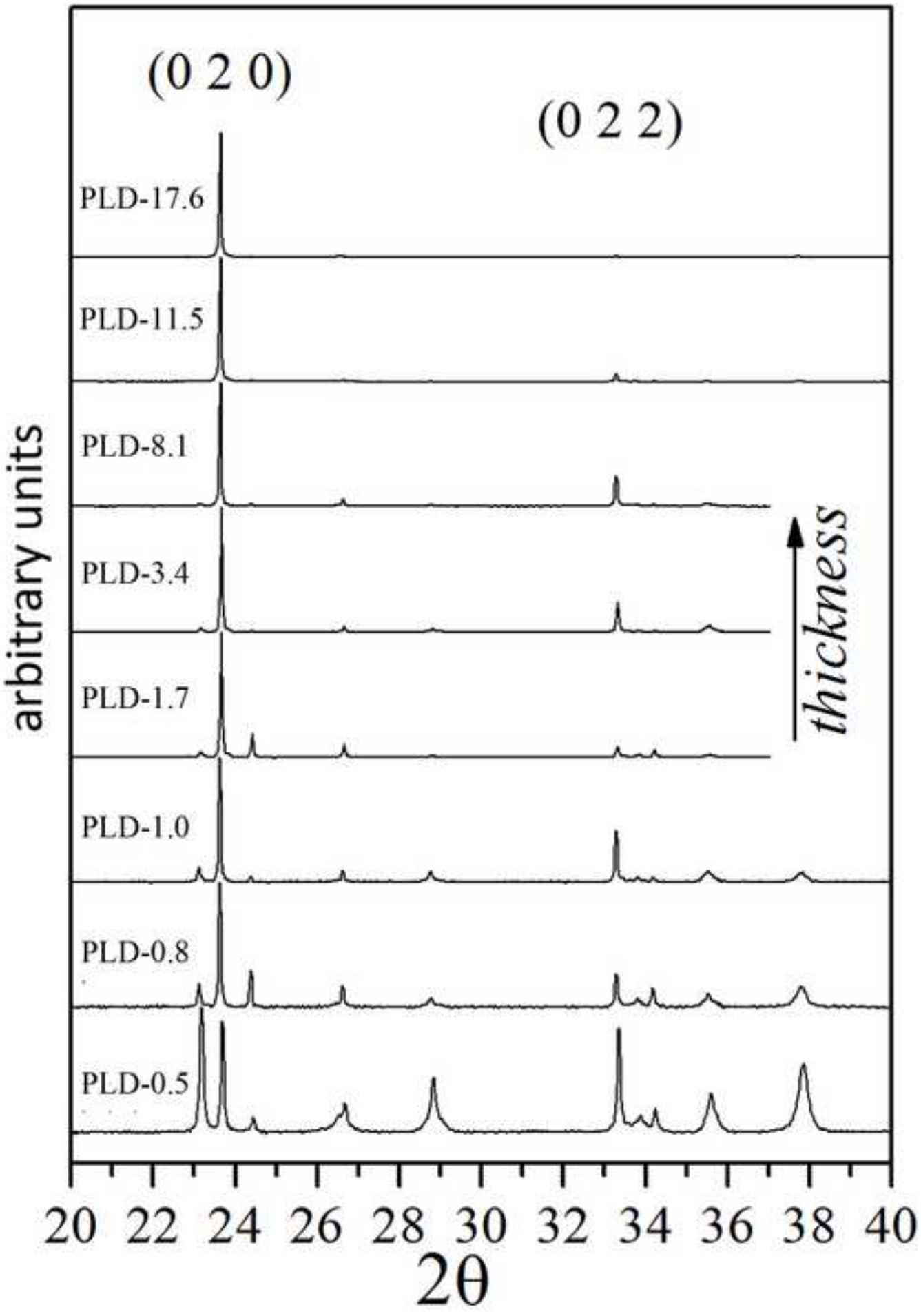

Figure 3
Click here to download high resolution image

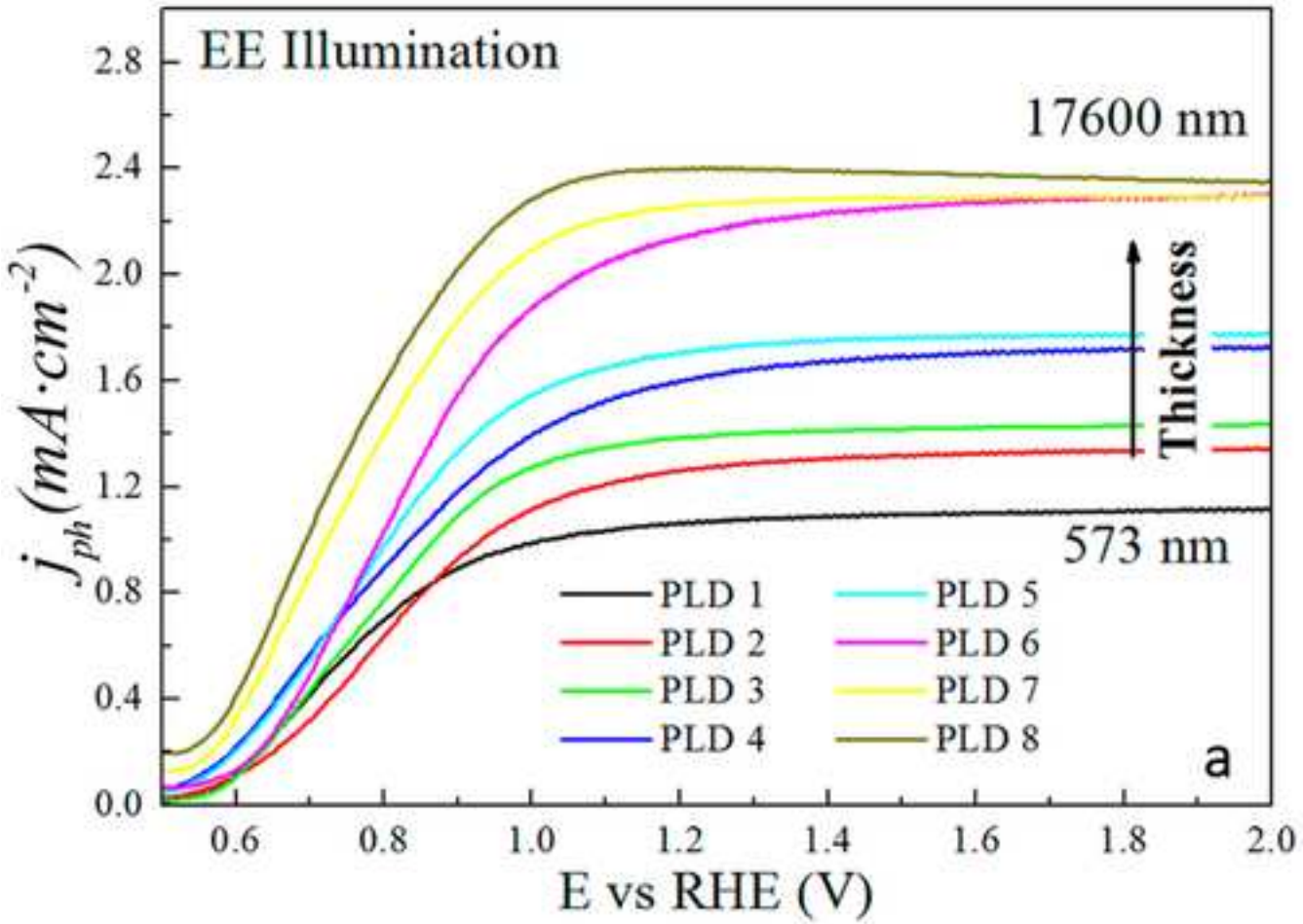

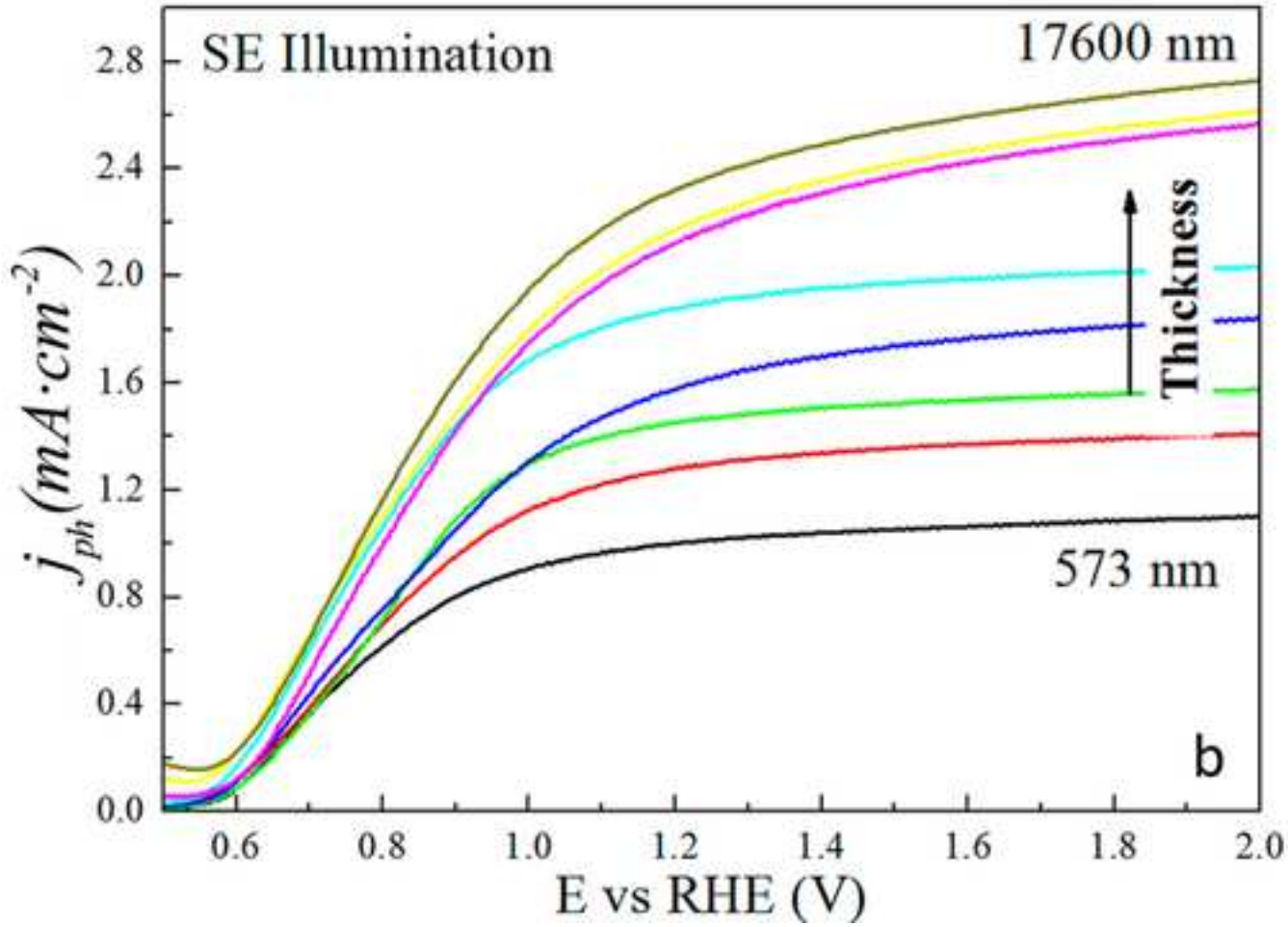

Figure 4
Click here to download high resolution image

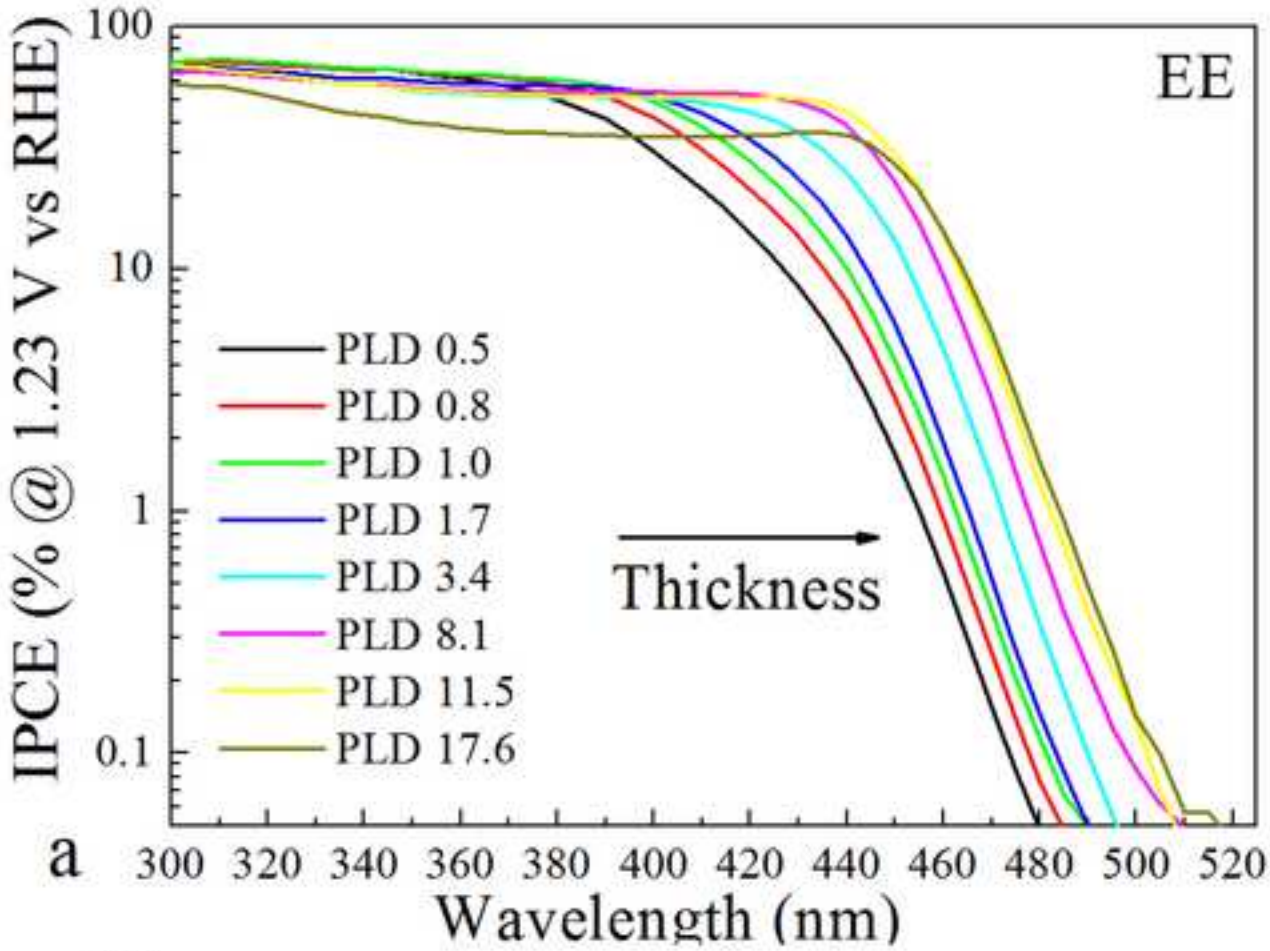

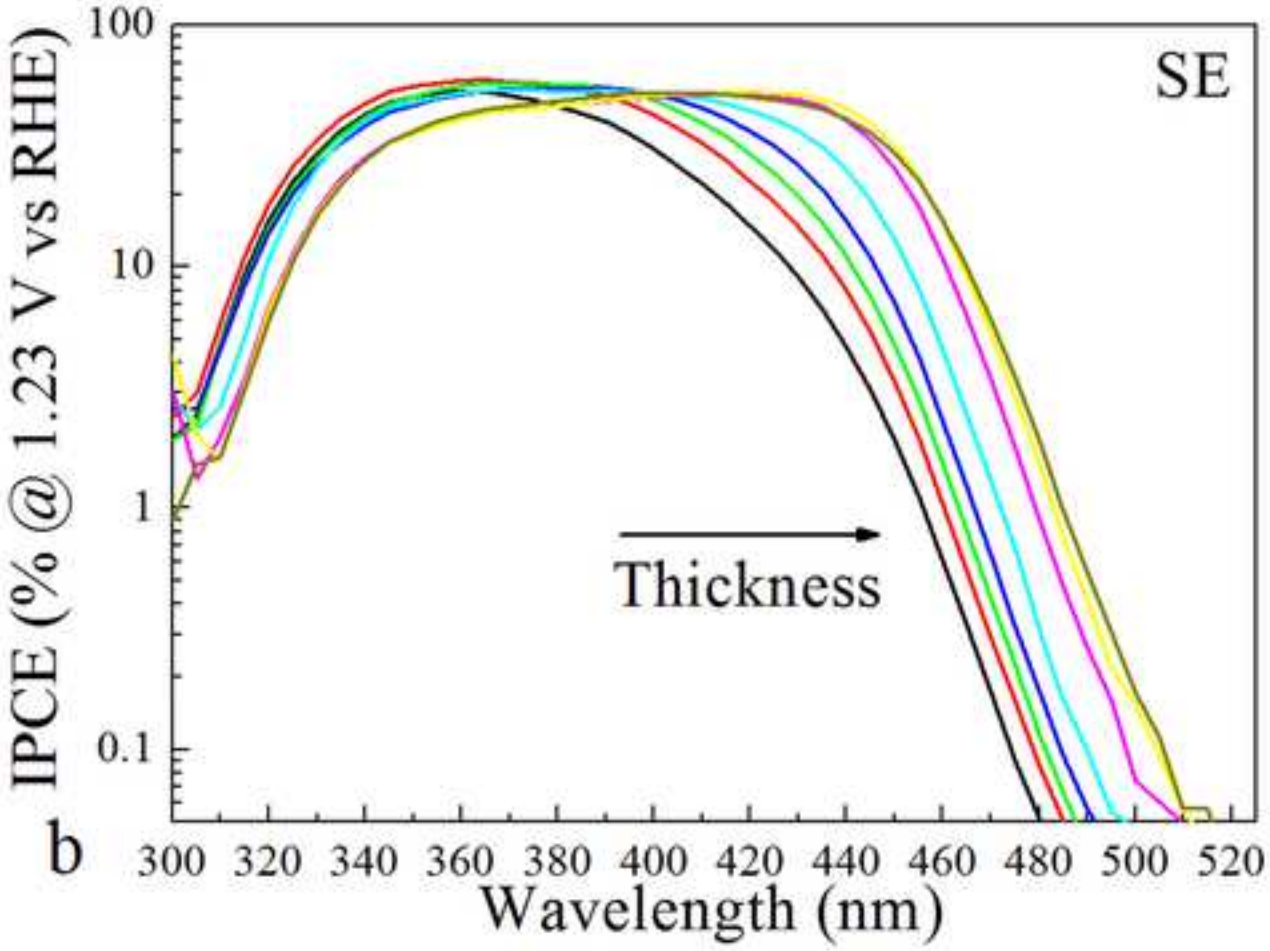

Figure 5

Click here to download high resolution image

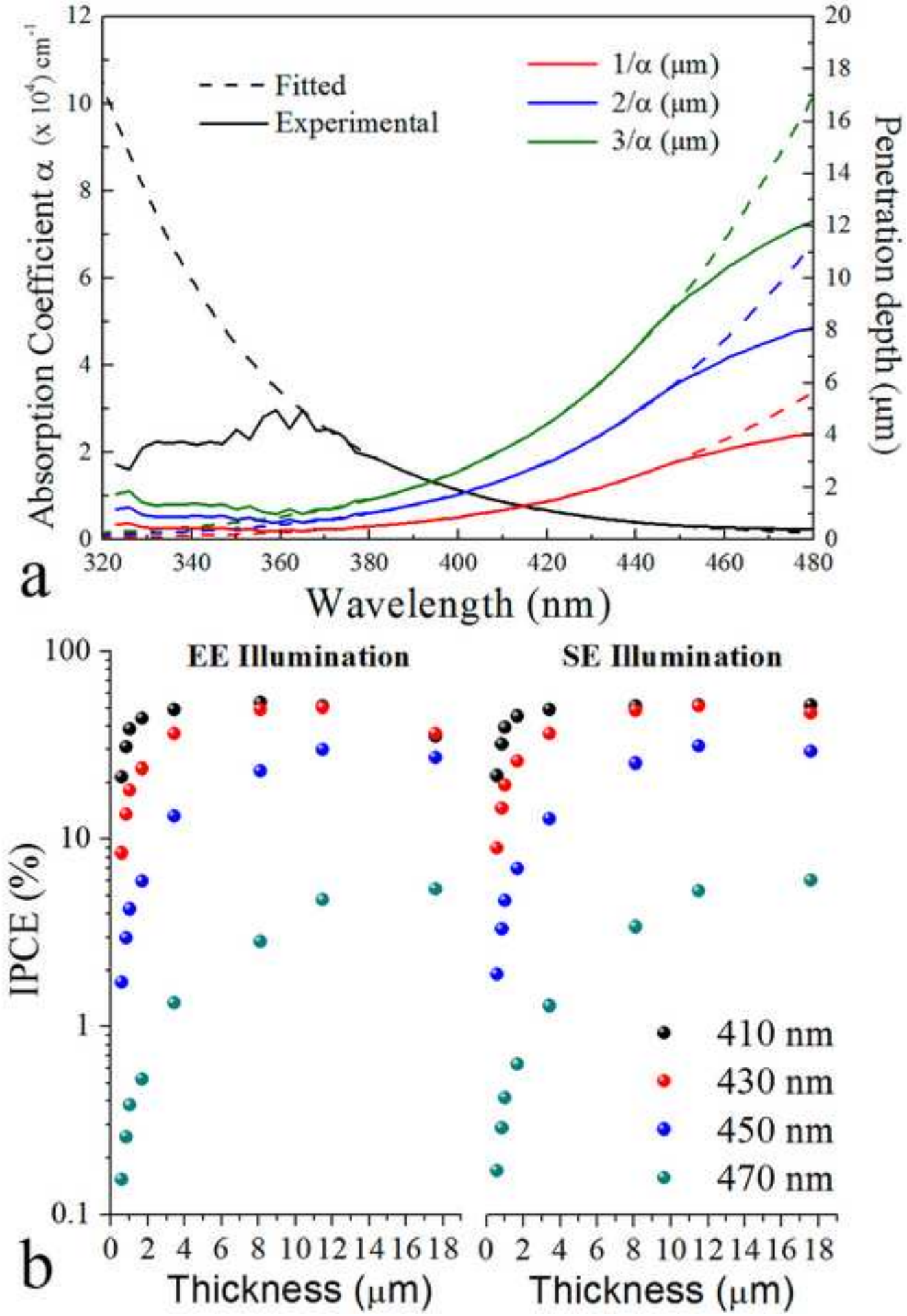

Figure 6

Click here to download high resolution image

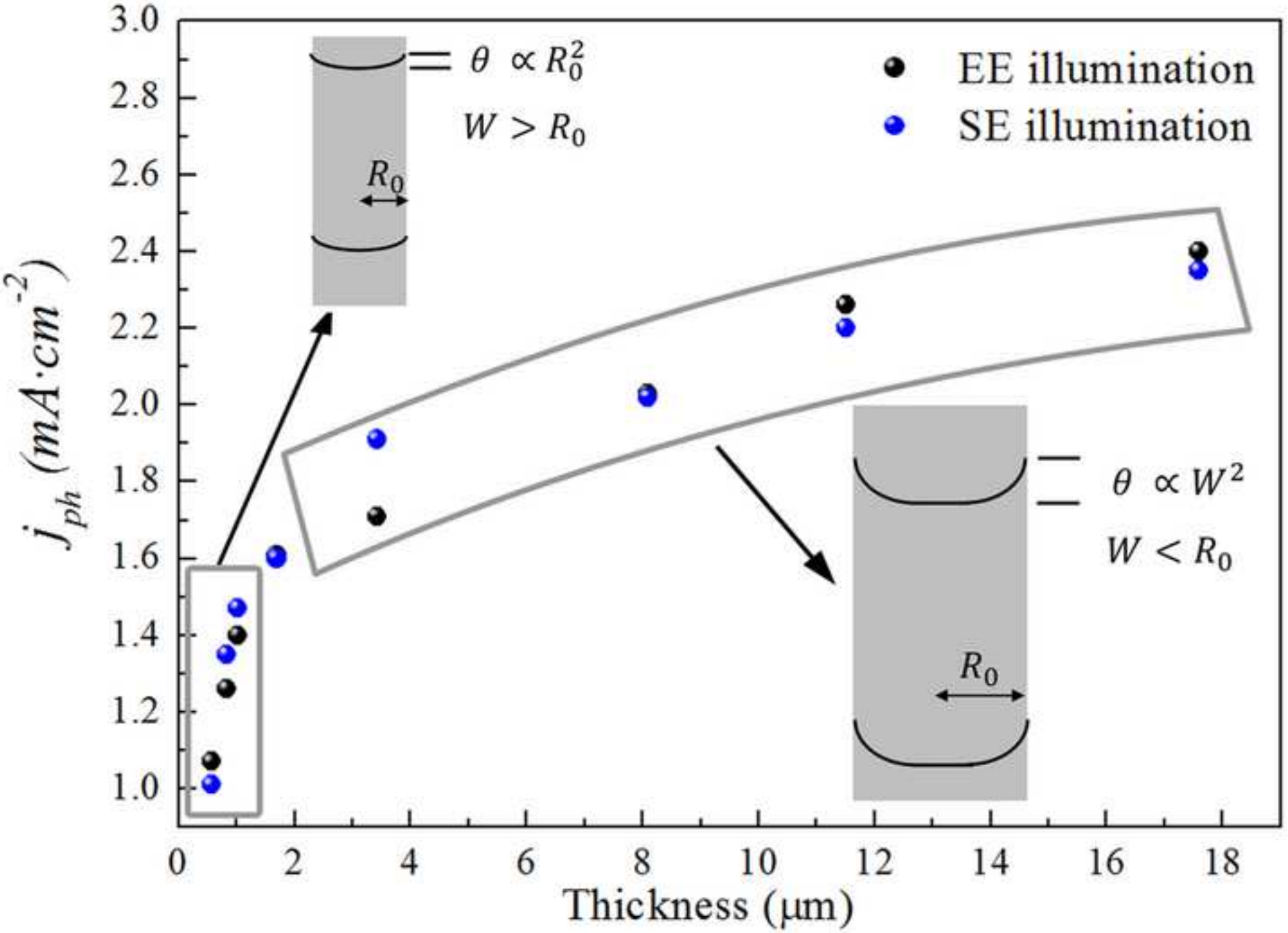

Figure 7

Click here to download high resolution image

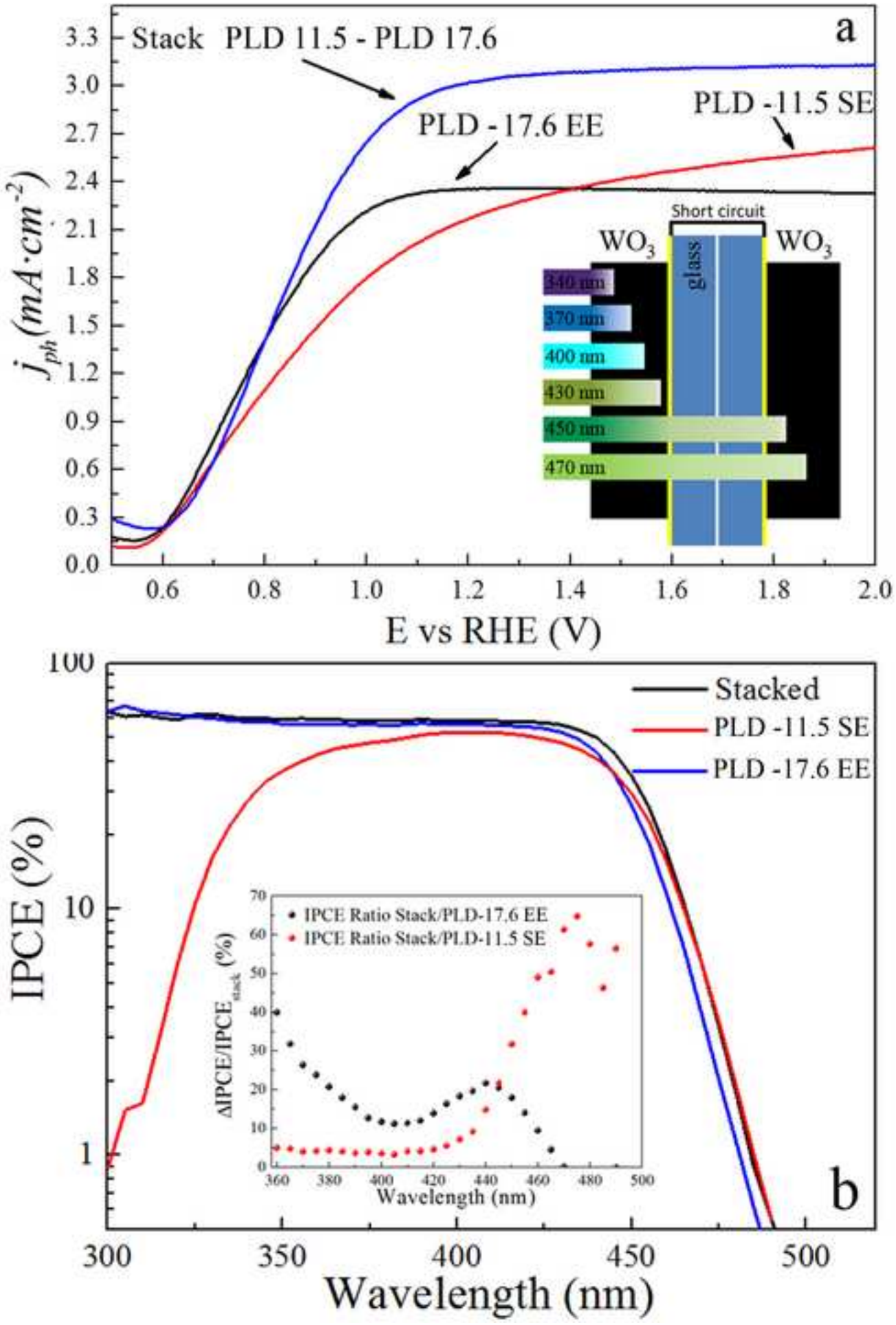

Figure 8

Click here to download high resolution image

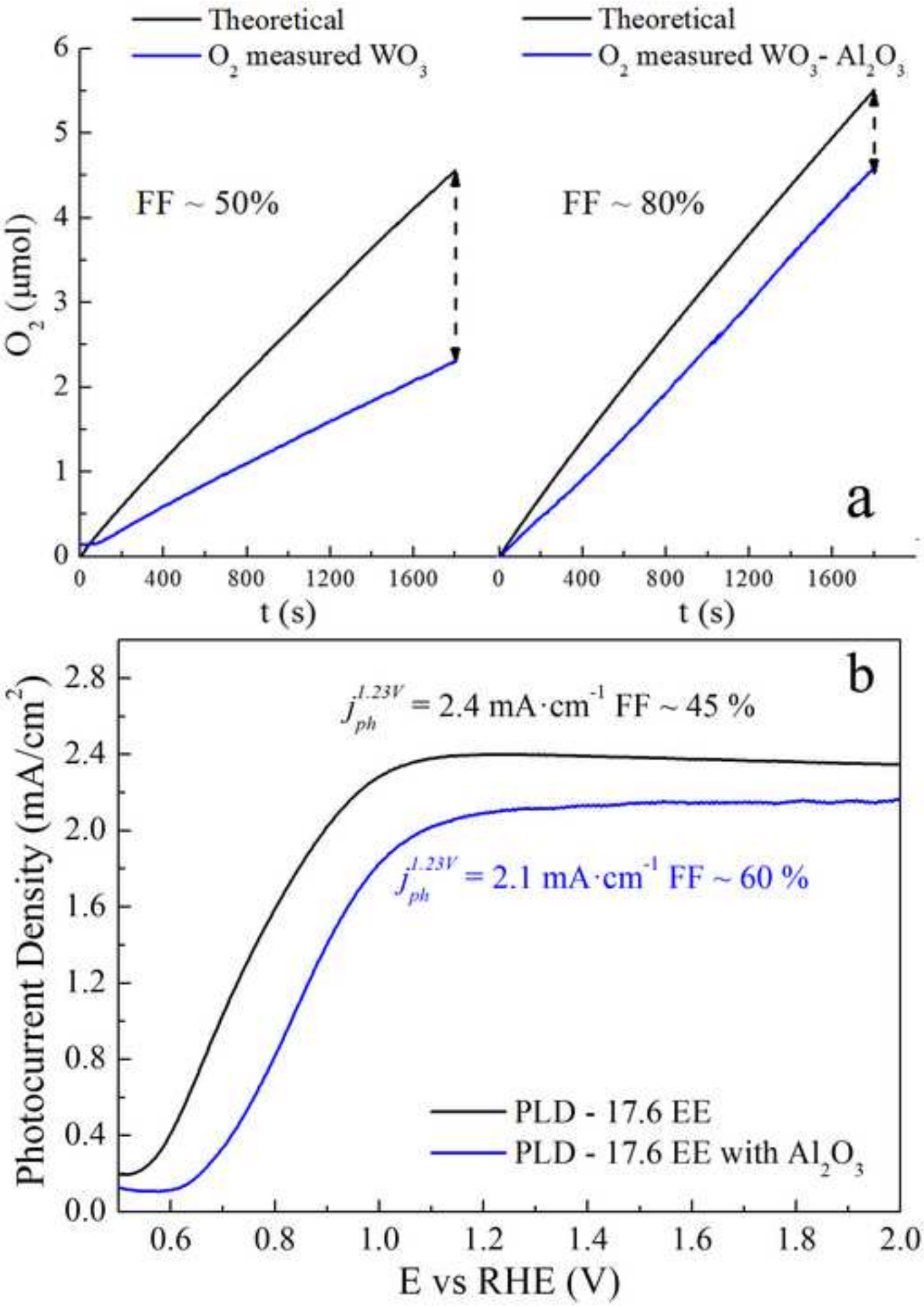

*Graphical Abstract

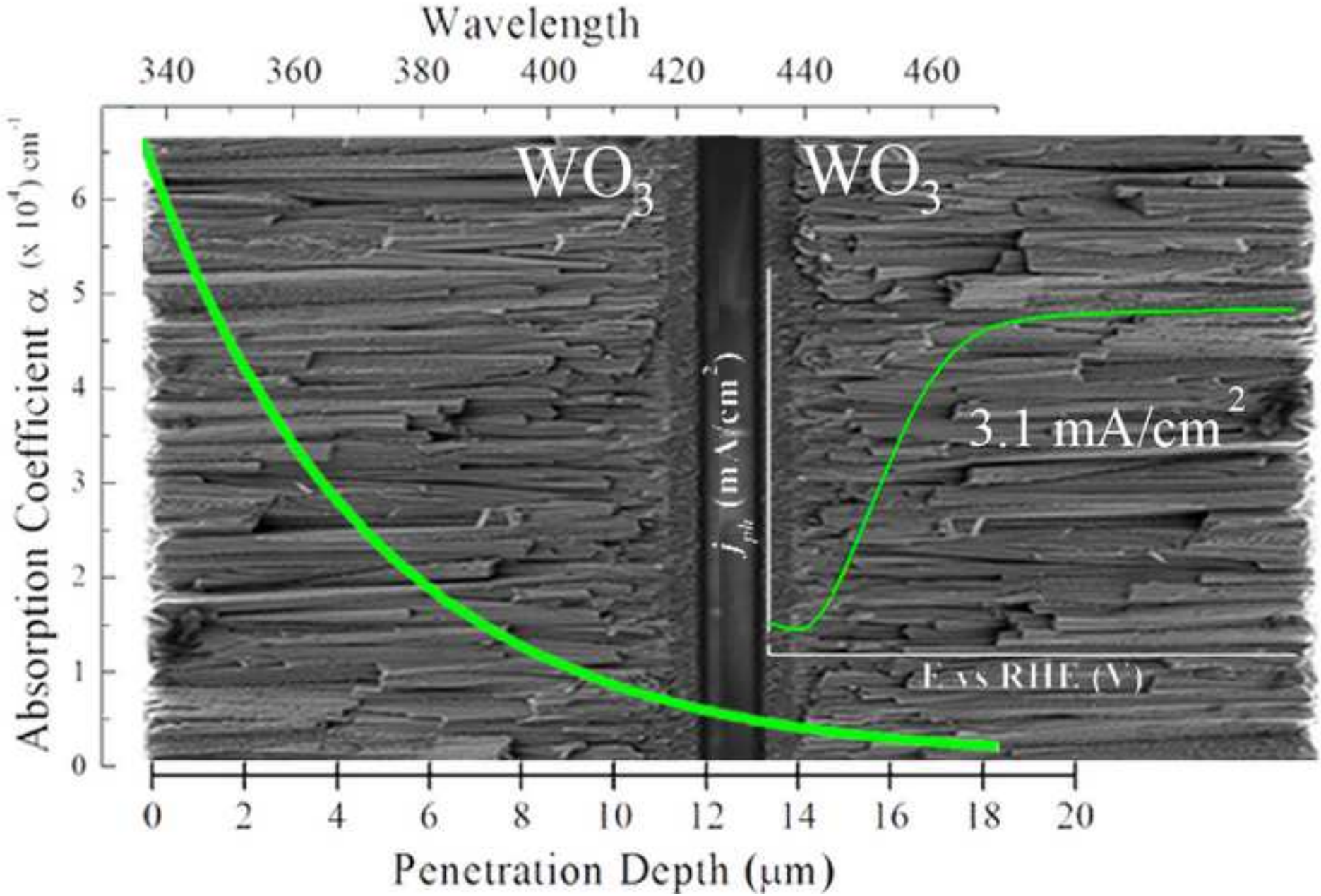

Highlights

- γ-monoclinic WO_3 were deposited by means of Pulsed Laser Deposition.
- WO_3 films showed a columnar shape structure, which resulted to be crucial in the photoanodes performances as the electrolyte was able to penetrate within the columns.
- A máximum photocurrent density up to 2.4 $mA \cdot cm^{-2}$ were achieved under 1.5 G irradiation.
- A new stack configuration is presented, which leads to unprecedented photocurrent density of 3.1 $mA \cdot cm^{-2}$ for unmodified WO_3 photoanodes.

Supplementary Material

Click here to download Supplementary Material: Supporting Information.pdf

Efficient WO_3 Photoanodes Fabricated by Pulsed Laser Deposition for Photoelectrochemical Water Splitting with high Faradaic efficiency.

C. Fàbrega[1,2,*], S. Murcia-López[1], D. Monllor-Satoca[1], J.D. Prades[2], M. D. Hernández-Alonso[3], G. Penelas[3], J.R. Morante[1,2], T. Andreu[1].

[1] Department of Advanced Materials for Energy, Catalonia Institute for Energy Research (IREC), Jardins de les Dones de Negre, 1, 08930 Sant Adrià de Besòs, Catalonia, Spain.
[2] Department of Electronics, Universitat de Barcelona (UB), Martí i Franquès, 1, 08028 Barcelona, Catalonia, Spain.
[3] Repsol Technology Center, Carretera de Extremadura A-5, km 18, 28935 Móstoles, Madrid, Spain.

[*]Corresponding author: Telf: +34934034804. E-mail: cfabrega@el.ub.edu (C. Fàbrega).

Abstract

In this work, we present a systematic study on the synthesis of monoclinic γ - WO_3 obtained using pulsed laser deposition (PLD). A photocurrent of 2.4 mA/cm^2 (60% of the optical maximum for a 2.7 eV gap material) was obtained for films as thick as 18 μm. FE-SEM images revealed that WO_3 films were actually formed by an array of oriented columns. Efficient hole extraction towards the electrolyte was observed and attributed to a possible accommodation of the electrolyte between the WO_3 columns, even for relatively compact films. This feature, combined with the detailed optical absorption and IPCE characterization, allowed us to implement a double-stack configuration of WO_3 photoanodes which resulted in a remarkable photocurrent density of 3.1 mA·cm^{-2} with 1 sun AM1.5G illumination in 0.1 M H_2SO_4 electrolyte. Faradaic efficiencies of more than 50% was obtained without co-catalyst, which is one the highest values reported for pure WO_3. By adding a 3 nm layer of Al_2O_3 by ALD, a faradaic efficiency of 80% was reached without diminishing the photocurrent density.

Keywords: Pulsed Laser Deposition; WO_3; water splitting; energy conversion; hydrogen production.

Manuscript

1. Introduction.

Photoelectrochemical (PEC) water splitting is still considered in contention for the most reliable technology for implementing the so-called solar-to-fuel economy [1]. Numerous efforts have been addressed to achieve a stable water photoelectrolysis system with materials able to absorb and convert the maximum amount of solar light. Among the materials of interest, metal oxides have centered most of the attention due to their inherent stability against photocorrosion, low cost, relative abundance, feasible scale up and mass production of PEC systems.

However, most of the traditional materials (i.e. TiO_2, Fe_2O_3 etc) are limited by their wide band gap [2,3] (TiO_2), poor electrical properties due to the very short hole life time [4] (Fe_2O_3) or improper band edge alignment for water splitting[1] (Fe_2O_3). Among them, WO_3 is recognized as one of the best positioned materials thanks to the wide range of synthetic process available [5–7] and the significant photon-to-current conversion efficiencies reported to date [8] for water oxidation. Other more complex materials like binary or ternary metal oxides, such as $BiVO_4$ [9–11], have emerged giving a new boost in the research of more efficient PEC systems. Similarly to Fe_2O_3, $BiVO_4$ [12] has deficient electrical properties and consequently, only thin films of tens of nanometers allow obtaining an efficient charge separation, resulting in a low solar light harvesting, limiting the overall performance. To overcome these constraints, some authors [13,14] opted by a different approach, implementing a host scaffold, or guest absorber, using WO_3. On top, thin films of $BiVO_4$ were deposited for an efficient charge separation at the interface of both materials and electron transport through the host material. For this reason, the development of these traditional materials is still of huge interest in spite of not fulfilling all the requirements for efficient PEC activity by themselves.

Another important aspect to consider, which is usually disregarded, is the reliability of the synthetic process in a large-scale scenario. Most synthetic processes are complex [12], involve

several steps [10] and their up scaling into large areas is not straightforward. This issue becomes much more evident in PEC devices made of different materials (e.g. host material, active material, blocking layers, catalyst, etc.), each one produced with different techniques [15].

Herein, we report on the synthesis of oriented and highly crystalline tungsten trioxide (WO_3) grown by Pulsed Laser Deposition (PLD) using preindustrial equipment able to process up to 4-inch-substrates with high uniformity and reproducibility. A complete and systematic study on the PLD growth parameters (e.g. oxygen pressure, temperature, number of pulses, etc.) allowed us to achieve one of the highest photocurrents densities in a water splitting system under simulated sunlight with pure WO_3 photoanodes, with an unprecedented synthesis ease and potential for scaling up. From the optical characteristics, IPCE and the film thickness optimization, we quantified some fundamental semiconductor features such as electrical transport properties, depletion region width and optical absorption coefficients (α). Additionally, a stack of two photoanodes is presented as a promising configuration to overcome the dichotomy between charge carrier collection and light absorption, typical in most metal oxide photoelectrodes. Finally, to improve the faradaic efficiency of our photoanodes two different strategies have been followed: alumina ALD coating and IrO_2 deposition.

2. Materials and methods.

2.1 Films deposition and OEC

Fluorine-doped tin oxide (FTO) glass substrates of 2 cm x 1.5 cm were used. Before deposition, glass pieces were cleaned with a subsequent sonication in acetone, isopropanol and double deionized water followed by a drying process with N_2 stream. WO_3 films were deposited by pulsed laser deposition (PLD) in a PLD 5000 equipment (PVD products Inc.) with a 240 nm excimer KrF laser. Substrates were placed facing down over a stainless steel shadow mask with a 1 cm x 1 cm square window. A commercial target (American Elements Inc.) was used as WO_3 source. The distance between the target and the substrate was kept at 90 mm for all depositions, and the frequency of the laser set at 10 Hz. Temperature, laser energy, number of pulses and oxygen pressure inside the chamber were used as control parameters to optimize for the PLD deposition. Samples names have been labeled PLD-X, where X is the approximate thickness of the sample in micrometers.

Alumina conformal coating were deposited by means of an Atomic Layer Deposition equipment from Cambridge NanoTech (Savannah). Trimethylaluminum (TMA) was used as aluminum source during the ALD process and water as an oxidizing agent. Growth temperature was fixed at 200◦C with a sequence of 2 ms of TMA followed by 2 ms of water. A total of 33 cycles were applied to obtain 3 nm of Al_2O_3, corresponding to a growth rate of 0.9 Å/cycle.

IrO_x deposition on the WO_3 electrode was performed by drop-casting. For this purpose, an IrO_x colloid was previously obtained by following the recipe reported in literature[16]. Firstly, 0.008 g of K_2IrCl_6 (Technical grade, Sigma-Aldrich) was added to 100 mL of Milli-Q water. Then, the necessary amount of a 0.5M NaOH solution was added until reaching a pH value of 12. After this, the mixture was heated at 80ºC until complete dissolution of the K_2IrCl_6. In a second step, this solution was cooled with an ice-bath at 5ºC and the pH value was adjusted again with a

0.5M HNO_3 solution to 8. Finally, the solution was heated at 80ºC for 30 min and a bluish IrO_2 colloid was obtained.

2.2 Characterization and Photoelectrochemical Measurements

The crystalline phase composition of the PLD products was determined by X-ray diffraction (XRD) measurements in a Bruker D8 Advance diffractometer equipped with a Cu Kα (1.54051 Å) radiation source, a LYNXEYE super speed detector, Bragg-Brentano configuration and a Ni filter. Optical characterization was performed in a Lambda 950 UV-Vis-NIR Spectrometer (PerkinElmer) equipped with a 150 mm Integrating Sphere and Spectralon standard. Transmittance and Reflectance measurements were separately carried out for each sample in a wavelength range of 300-800 nm, with a step of 5 nm. The morphology of the as-prepared samples was observed by field-emission scanning electron microscopy (FE-SEM, Zeiss Auriga). Thicknesses of the samples were measured by profilometry with a KLA-Tencor P15 equipment with a low force head. 3D images were obtained with a Sensofar non-contact optical 3D confocal interferometer. Photoelectrochemical (PEC) measurements were conducted in a three-electrode quartz cell connected to a Parstat 2273 potentiostat. A 0.1 M H_2SO_4 solution was used as electrolyte, a Pt mesh as counter electrode and Ag/AgCl (3 M) ($E^º$ = 0.203 V vs NHE) as reference electrode. The results are presented against the reversible hydrogen electrode (RHE), calculated from the Nernst equation. Cyclic voltammetries with a sweep rate of 40 $mV \cdot s^{-1}$ were recorded in the dark and under illumination with simulated AM1.5G solar light provided by a portable solar simulator (Peccell, PEC-L01).

The incident photon to current conversion efficiency (IPCE) was measured at a constant bias of 1.23 V vs RHE in a 0.1 M H_2SO_4 electrolyte using a wavelength range of 300 to 550 nm with an interval step of 5 nm and a stabilization time of 2 minutes between measurements, with a light on-off time cycle at each wavelength of 90 s and 30 s, respectively. Monochromatic illumination was supplied by a LS Xenon Light Source (ABET technologies) connected to an

Oriel Cornerstone 260 1/4m monochromator. Photon flux was estimated by calibrating the monochromatic light with a Silicon Photodiode (Thorlabs, S120VC).

The O_2 concentration in the anolyte was monitored with a fiber optical oxygen transmitter Fibox 3 trace V3 (PreSens). The device is equipped with two sensors: a sensor coating type PSt3 (detection limit 15 ppb) and a temperature sensor for compensation during the tests. Previous degasification of the three-electrode cell (without head space) with N_2 flow was performed, after which the electrodes were illuminated (AM1.5 G, 1 Sun) during 30 min at 1.23V vs RHE. The baseline drift in the O_2 concentration was estimated immediately before and after the (photo)electrolysis and was compensated in each experiment by linear extrapolation.

3. Results and discussion.

Among all polymorphs, γ-WO_3 monoclinic is the most stable and photoactive phase. This crystal structure is very sensitive to both temperature and defects, i.e. oxygen vacancies [17]. A preliminary study on the effect of substrate temperature and oxygen partial pressure in the PLD chamber was performed in order to determine the optimal deposition parameters. Photoelectrochemical measurements showed that 400ºC and 100 mTorr of partial oxygen pressure provided the best performing samples (S1). All films deposited in a temperature range from 300 to 600ºC and oxygen partial pressure from 50 to 200 mTorr presented monoclinic structure (S2). At lower oxygen pressures, the layers were highly reduced looking black colored and displaying almost no photoactivity.

WO_3 film thickness was optimized by fixing substrate temperature and oxygen pressure at 400ºC and 100 mTorr respectively, while increasing the number of pulses and/or the nominal energy of the laser between 300 and 550 mJ. It was found that only the deposition rate was affected by the laser energy. A perfect correlation between thickness and the total amount of energy (i.e. product of number of pulses and laser energy) with a rate of 5400 mJ per nanometer was determined (S3). Samples with thicknesses ranging from 573 nm to more than

17 μm were fabricated (Table I). A 3D reconstruction with the confocal microscope showed uniform thicknesses through the entire 1 cm x 1 cm samples (S4).

Field Emission Scanning Electron Microscopy images (Figure 1) showed that the surface of WO_3 grown by PLD was uniform and finished with a pyramidal-like pattern. A detailed view of a SEM cross section revealed that in fact, these WO_3 films consisted of an array of oriented compact columns (Figure 1). This apparent orientation was confirmed by XRD analysis (Figure 2). As WO_3 thickness increased, all reflections except the (002) of the monoclinic phase started to disappear, which implies the predominance of this orientation.

Figure 3 shows the photocurrent density versus potential curves for all WO_3 films with different thicknesses, measured in 0.1 M H_2SO_4 electrolyte under AM 1.5G irradiation (100 mW cm^{-2}) from both front (EE) and back (SE) illumination. Open circuit voltages were in all cases around 0.5 V vs RHE and current densities increased with increasing WO_3 thickness, reaching a photocurrent density of 2.4 $mA \cdot cm^{-2}$ at 1.23 V vs RHE for the thickest sample (17.6 μm), which is one of the highest photocurrent densities for WO_3 photoanodes reported to date [5,17,18]. Bearing in mind that optically WO_3 could achieve a maximum of 4.0 $mA \cdot cm^{-2}$ (2.7 eV bandgap) [19], this represents a 60% of the optical maximum, that has been achieved in the absence of additional structural (i.e. doping) or surface modifications (e.g. plasmonic nanoparticles, heterojunctions, passivation, etc).

To gain further insight into the mechanistic aspects of the charge transfer phenomena, the IPCE of all samples (Figure 4) were recorded at 1.23V vs RHE under EE and SE illumination. A summary of the photocurrent densities, calculated by convoluting the IPCE with the AM 1.5G solar irradiation spectra (S5), can be found in Table I. The first thing to note from the IPCE spectra (Figure 4) is the notorious decrease in the region between 300 and 340 nm when illuminating from the back side due to the absorption of light by the FTO layer. At the same time, huge improvements in the IPCE values at long wavelengths (390-480 nm) were found

due to the increased absorption capability of thicker WO_3 films, as shown in the UV-vis spectra (S6). To determine the absorption coefficient, we deposited a WO_3 layer over a quartz substrate in order to avoid the FTO absorption. From the transmittance and reflectance spectra, the absorption coefficient was inferred. Along with the absorption coefficient spectrum, we plotted the corresponding penetration length, considering 63%, 83% and 95% of the absorbed light (Figure 5a). The absorption coefficient cannot be properly estimated in the region of short and long wavelengths and, for that reason, we restrained the experimental fitting to the 380-440 nm range.

It is clear that the absorption coefficient of WO_3 is quite low compared to other materials (e.g. 10^5 to 10^6 cm^{-1} for hematite [20]) , which implies that thicker films are needed if fully absorption of the solar spectrum above the band gap is required. For example, for a wavelength close to the band gap of WO_3 (460 nm), a 4 μm thick layer is needed to absorb 63% of this light; and a 12 μm thick one to absorb 95%. The absorption profile is remarkably coincident with the IPCE values obtained for increasing thicknesses of WO_3 films (figure 5b): the maximum value of the IPCE at each wavelength is reached, in both EE and SE illumination, when WO_3 film thickness is above the penetration depth corresponding to 95% absorption. Remarkably, IPCE values of up to 70% are reached, in line with mesoporous WO_3 thick films with randomly oriented nanoparticles [17].

Of course, light absorption is not the only important parameter to be taken into account in order to obtain top performance photoanodes. Separation and transport of the photogenerated charge carriers must be considered. For example, considering that upon front illumination shorter wavelengths are absorbed within the first 2 μm, in case of thicker samples, electrons must still flow along several μm to reach the FTO back contact, which implies that electron transport is dominated by diffusion in a similar fashion to the Södergren model for microporous semiconductors [21]. Thus, an estimated minimum apparent diffusion length of

15 μm can be inferred. These values of electron diffusion lengths [22] are in the same order of magnitude that of the ones obtained for TiO_2 in dye sensitized solar cells [23], which generally have values that could even exceed the electrode thickness. Assuming that this is the case of our films [17], from the Södergren model it can be inferred that the diffusion length is 2 to 3 times larger than the electrode thickness (S7). Accordingly, a lower (bulk) recombination rate for both thin and thick films could be invoked to justify such large diffusion lengths [24]. However, in the case of back illumination, at short wavelengths (300 - 380 nm) electrons can also be generated in abundance close to the FTO contact and holes must travel long distances. Hole diffusion at micron distances is highly unlikely (diffusion length L_p in WO_3 is around 400 nm [25]). A possible explanation to the high photocurrent observed with back illumination (and thus a high hole collection in the electrolyte) involves the structure of the WO_3 layers: the column-like structure can be penetrated by the electrolyte leading to shorter distances between the hole generation sites (inside the WO_3 columns) and the hole collector (electrolyte). In this way, holes can be efficiently separated and transferred to the electrolyte (which would be at reach right after photo generation), while electrons can diffuse inside WO_3 columns for longer distances.

To prove that the electrolyte effectively penetrates into the WO_3 layers, the amount of accumulated/extracted charge was determined by integrating dark voltammetries for each thickness (S8). The capacitive behavior of a voltammetry in the dark relates to the insertion-deinsertion of cations in charge accumulation (i.e. negative polarization). As the cation insertion occurs at the electrolyte/electrode interface, the charge can be directly correlated to the electrochemically active surface area of the material. In compact flat films, total charge values should be less dependent of the film thickness. In the present case, the total charge increases with the film thickness (S8), which implies that a larger WO_3 surface is in contact with the electrolyte for thicker samples.

In this regard, it is interesting that considering the IPCE values at a given wavelength for different sample thicknesses, one may observe that at shorter wavelengths the increment of the IPCE values is very strong, up to almost 2 µm thick samples (Figure 5b). A similar trend can be observed in the plot of the photocurrent density as a function of the WO_3 film thickness (Figure 6). These two different regimes (a steep increase up to 2 µm and a slower one from there on) can be explained taking into account the extension of the surface depleted region. It is well known that the depletion region in a semiconductor is the key factor for efficient charge carrier separation [26]. In a first approximation, the Poisson equation can be analytically solved for planar, cylindrical and spherical structures [27]. For each structure (i.e. in 1D, 2D and 3D respectively) there is a characteristic dimension, or a geometrical parameter (R_0), that rules the dependence of the potential drop within the depletion region. These R_0 parameters are the thickness, for planar structures, and the radius for the cylindrical and spherical ones. In all cases, one can distinguish two different regimes: (I) when the depletion region (W) is shorter than the characteristic dimension (R_0) or (II) when it is longer [27]:

$$\theta \propto R_0^{\,2} \qquad \text{for } W \leq R_0 \qquad (1)$$

$$\theta \propto W^2 \sim ct. \qquad \text{for } W > R_0 \qquad (2)$$

where θ is a dimensionless variable that is related to the potential drop at the semiconductor surface (measured with respect to the center of the semiconductor) given by $\theta = e\phi_{SC}/kT$, where k is the Boltzmann constant (1.38×10^{-23} J·K^{-1}), ϕ_{SC} is the potential in the space charge region (E - E_{fb}, where E_{fb} is the flat-band potential) and T is the absolute temperature in K. From these expressions, it is clear that when W < R_0 the potential increases quadratically with the radius. Thus, the electron-hole separation capability and the resulting photocurrent increase rapidly as well. In contrast, when W > R_0 the potential drop remains steady in a

maximum value (corresponding to the value at W = R_0), which is independent on the geometrical parameter.

In our case, the PEC layer was made of independent WO_3 nanorods with a depleted shell. Therefore, the geometrical parameter is the diameter of the nanorods formed during the PLD process. When increasing the number of PLD pulses, not only the nanorods get longer, but also their diameter increases. Consequently, the first regime corresponds to thinner films (i.e. thinner nanorods) in which the voltage drop inside the depletion region can increase steeply, dominated by the quadratic relationship with the radius (Eq. 1), up to a maximum value. When the potential drop is maximum, i.e. the diameter of the nanorod is enough to develop completely the electric field related to the depletion region, charge separation is not further improved. From then on, IPCE and photocurrent density increase more slowly, only affected by the increase in the amount of the absorbed light or the exposed surface area to the electrolyte. Indeed, if we correlate the photocurrent values with the relative charge of the electrodes (as a measure of the surface area from dark voltammetry), we observe a similar correlation to that of the depletion layer width, pointing out that the surface area is also crucial in determining the final photoactivity yield of the electrodes (S9).

In order to tackle the optimizacion of light absorption by the material, a stack of PLD-11.5 and PLD-17.6 samples was built (keeping the WO_3 layers in the outer side, as shown in the inset in Fig. 7a) seeking the full absorption of the solar light by WO_3 layer while preserving the good charge extraction properties observed in these samples separately. *j-E* curves of Figure 7a show that the stacking of both samples resulted in a maximum photocurrent density of 3.1 $mA \cdot cm^{-2}$ (78% of the optical maximum for WO_3), which means an increase of almost 30% with respect to PLD-11.5 and PLD-17.6, separately. According to the characterization of the individual WO_3 photoanodes, it is likely that longer wavelengths were partially transmitted through the first WO_3 film and reabsorbed by the second one. Although only a small

percentage of these long wavelengths were transmitted, their contribution to the total photocurrent can be very important considering that the irradiance at longer wavelengths is greater than at shorter wavelengths. Figure 7b presents the relative increment of the spectral response (IPCE) of each component (PLD -11.5 and PLD – 17.6) with respect to the measured IPCE of the double-stacked sample. Comparing the results of the stack with sample PLD–17.6 EE, an increment of up to 50% was achieved in the range from 440 nm to 475 nm and only 3% in the remaining range. In contrast, the ratio between PLD – 11.5 SE and the stacked configuration showed a decrease from 440 nm onwards, indicating that PLD – 11.5 SE is the main responsible of the absorption of light at long wavelengths. The increase at short wavelengths is only due to the absorption of light by the FTO/glass substrates when illuminated from the back. For this reason, the spectrum was truncated below 360 nm.

This stacking approach is especially attractive for semiconductors where electron and hole transport properties are a limiting factor in thick films, as shown by Itoh et al. for thin hematite films [28]. For example, it is well known that Fe_2O_3 [29] and $BiVO_4$ [25] display poor electrical properties and high recombination rates. Film thickness around 40-150 nm (or even less in the case of Fe_2O_3) are typical values for the best performing photoanodes [30,31]. As light penetration depth in these materials is as long as 500 nm for longer wavelengths, most of the light is transmitted and lost. Thus, double side configurations as the one proposed in this work offer a straight forward path to enhance the light collection capabilities, without worsening the transport properties. As such, with the transport and light absorption hassles solved, the photoanode optimization lies in the surface reactivity and the hole transfer efficiency to the species at the interface of the electrolyte.

Finally, in order to determine the faradaic efficiency of the oxygen evolution reaction (OER), the O_2 concentration was measured with an optical O_2 sensor. To that end, several WO_3 samples with around 1.7 μm thickness were fabricated. It is well known that, in general, wide

band gap semiconductors might reduce the counter-anions present in the electrolyte rather than reduce water to produce oxygen [32,33]. Particularly, WO_3 has shown faradaic efficiencies of around 30% or less due to the formation of peroxo species and/or reduction of counter anions [6,34] . Several strategies have been followed with the aim of improving the OER faradaic efficiency. Kim et al.[6] demonstrated that an alumina coating of only few nanometers is enough to hamper most of the competing reactions, yielding a faradaic efficiency of 50%. In line with that work, a 3 nm ALD coating of alumina was applied on one of the PLD WO_3 samples fabricated for this purpose. Notably, the photoactivity was slightly improved by the ALD deposition (S10). In our case, the bare WO_3 sample showed a 50% of faradic efficient (Figure 8), which is already much higher than the faradaic efficiency reported elsewhere with bare WO_3. However, by introducing a 3 nm ALD layer of Al_2O_3 on top of the WO_3, the faradaic efficiency reached almost 80% (Figure 8a). This outstanding result is of tremendous relevance, as usually, expensive and scarce materials, such as Iridium, are needed to obtain acceptable values of faradaic efficiency for the oxygen evolution reaction in acid electrolyte.

To further evaluate the reliability of the Al_2O_3 as a catalyst for the oxygen evolution reaction, a 3 nm layer were deposited on top of the thickest WO_3 sample (PLD – 17.6). Although a faradaic efficiency of 60% was achieved with this procedure (Figure 8b), which supposed an increase respect to the bare sample (FF = 45%), the numbers obtained with thinner samples were considerably higher (65-80%). Furthermore, the photocurrent density was slightly hampered by the presence of the alumina layer, decreasing form the original 2.4 $mA \cdot cm^{-2}$ to 2.1 $mA \cdot cm^{-2}$. A plausible explanation, in the absence of further study, is that the deposition conditions of the ALD alumina layer must be adapted for an efficient conformal coverage in samples with very high aspect ratios and very small porous, as is the case of the PLD – 17.6 compared with the previous samples with only 1.7 μm thickness.

4. Conclusions.

Monoclinic γ-WO_3 films were successfully deposited on FTO substrates by pulsed laser deposition. These films showed a columnar-shape structure, which resulted to be crucial in the photoanodes performances as the electrolyte was able to penetrate within the columns contributing to improve the charge transport. As the electrolyte was in contact with the walls of the WO_3 columns, holes path lengths were low enough for an efficient injection into the electrolyte. On the other hand, it has been demonstrated that electrons, with much longer diffusion lengths, were able to travel the whole electrode thickness to reach the FTO back contact. Both efficient hole injection into the electrolyte and long electron diffusion lengths were essential because of the low absorption coefficient of WO_3. By virtue of their morphology, thick films fabrication were attainable in order to collect and absorb the maximum amount of solar light, obtaining remarkably high photocurrent densities, up to 2.4 $mA \cdot cm^{-2}$ (60% of the optical maximum). Furthermore, to ensure a full absorption of the light, a new configuration has been presented in the form of two stacked WO_3 samples. In this configuration, 3.1 $mA \cdot cm^{-2}$ were obtained (78% of the optical maximum), which is one of the highest photocurrent densities reported for unmodified WO_3 photoanodes. Likewise, a faradaic efficiency of more than 50% was obtained without co-catalyst WO_3.

By adding a 3 nm layer of Al_2O_3 by ALD, a faradaic efficiency of 80% was reached without diminishing the photocurrent density. However, for thicker samples, both faradaic efficiency and photocurrent density were hampered by the presence of the alumina layer. A further study is necessary in order to determine the proper deposition conditions to obtain the same performances for thicker samples.

PLD proved to be a suitable technique for the deposition of metal oxide films on large areas, even those with a much more complex stoichiometry thanks to the perfect transfer from target to substrate.

5. Acknowledgements

This work was supported by Repsol, S.A. IREC also acknowledges additional support by the European Regional Development Funds (ERDF, FEDER Programa Competitivitat de Catalunya 2007-2013), by MINECO project ENE2012-3651, MAT2014-59961-C2-1-R and Multicat (CSD2009- 00055), and the Framework 7 program projects SOLAROGENIX (FP7-NMP-2012-310333) and CEOPS (FP7-NMP-2012-309984). J.D. Prades acknowledges the support from the Serra Húnter Programme.

Figure Caption

Figure 1 Top view and cross section FE-SEM images showing the characteristic pyramidal-like shape and the columnar orientation of a WO_3 PLD deposited on an FTO substrate.

Figure 2 XRD spectra for all samples with increasing thickness. Two reflections of WO_3 monoclinic phase are indexed, (020) and (022), showing that a preferential growth through (020) crystallographic planes is obtained in our PLD deposited samples.

Figure 3 Photocurrent density obtained under 100 $mW \cdot cm^{-2}$ simulated sunlight from both, **(a)** front (EE) and **(b)** back (SE) illumination. All measurements were recorded at a scan rate of 40 $mV \cdot s^{-1}$ using an Ag/AgCl reference electrode in a 0.1M H_2SO_4 electrolyte. Potential have been referred to the reversible hydrogen electrode (RHE). Measured dark currents of all samples were below 50 $\mu A \cdot cm^{-2}$ (not plotted).

Figure 4 (a) Front (EE) and **(b)** back (SE) illumination IPCE spectra recorded at 1.23 V vs RHE in a 0.1 M H_2SO_4 electrolyte using a wavelength range of 300 to 550 nm with an interval step of 5 nm and a stabilization time of 2 minutes between measurements (light on, 90 s; light off, 30 s).

Figure 5 (a) Absorption coefficient calculated from the UV-vis spectra and the corresponding penetration depth considering 63% ($1/\alpha$), 83% ($2/\alpha$) and 95% ($3/\alpha$) of absorbed light. Dashed lines correspond to fittings made in the intermediate region of the spectrum (380-440 nm) because the experimental data in high and low absorption regions were not accurate. **(b)** IPCE as a function of WO_3 film thickness at different wavelengths (410, 430, 450 and 470 nm) with front (EE) and back (SE) illumination.

Figure 6 Photocurrent density as a function of WO_3 thickness. Two regions with different trends are highlighted showing the transition between an almost fully depleted films with a lower potential drop ($W > R_0$) and the classical potential drop expression in a semiconductor ($W < R_0$).

Figure 7 (a) Photocurrent density under 100 $mW \cdot cm^{-2}$ simulated sunlight of a double stacked configuration compared with the corresponding individual WO_3 photoelectrodes (PLD – 17.6 EE and PLD – 11.5 SE). All measurements were recorded at a scan rate of 40 $mV \cdot s^{-1}$ using an Ag/AgCl reference electrode in a 0.1M H_2SO_4 electrolyte. Potential have been referred to the reversible hydrogen electrode (RHE). Measured dark currents of all samples were below 50 $\mu A \cdot cm^{-2}$ (not plotted). **(b)** IPCE of PLD-11.5 and PLD–17.6 and the corresponding stacked configuration. (Inset) Relative IPCE increment of PLD-11.5 and PLD–17.6 with respect to the stacked configuration as a function of wavelength. The spectra have been truncated at 360 nm because the relative IPCE between the stack and PLD–11.5 SE is strongly affected by the absorption of light through the FTO/glass substrate.

Figure 8 (a) Oxygen evolution reaction faradaic efficiency of a bare WO_3 sample, an ALD coated sample with 3 nm of alumina. **(b)** *j*-E curve and the corresponding faradaic efficiency of PLD – 17.6 sample with and without alumina co-catalyst.

Table I. Summary of electrode thicknesses and photocurrents for all prepared films

Sample	Thickness* ±10 (nm)	J_{ph}(EE)** ±0.01 (mA·cm^{-2})	J_{ph}(SE)** ±0.01 (mA·cm^{-2})	EE-IPCE @350 nm ±0.1 (%)	EE-IPCE @450 nm ±0.1 (%)	SE-IPCE @350 nm ±0.1 (%)	SE-IPCE @450 nm ±0.1 (%)
PLD – 0.5	*570*	*1.07*	*1.01*	*64.8*	*1.7*	*50.4*	*1.9*
PLD – 0.8	*840*	*1.26*	*1.35*	*65.0*	*2.9*	*55.6*	*3.3*
PLD – 1.0	*1030*	*1.40*	*1.47*	*65.3*	*4.2*	*50.7*	*4.7*
PLD – 1.7	*1700*	*1.61*	*1.60*	*59.7*	*5.9*	*46.9*	*7.0*
PLD – 3.4	*3420*	*1.71*	*1.91*	*54.9*	*13.2*	*48.1*	*12.9*
PLD – 8.1	*8100*	*2.03*	*2.02*	*55.9*	*23.0*	*35.9*	*25.5*
PLD – 11.5	*11500*	*2.26*	*2.20*	*55.1*	*30.1*	*35.6*	*31.6*
PLD – 17.6	*17600*	*2.40*	*2.35*	*40.3*	*27.2*	*36.5*	*29.5*

* Thickness was measured using a KLA-Tencor P15 profiler.

** Photocurrent density was measured from *j-E* curves at 1.23 V vs RHE with 1 sun AM1.5G illumination in 0.1 M H_2SO_4 electrolyte.

References

[1] Z. Li, W. Luo, M. Zhang, J. Feng, Z. Zou, Photoelectrochemical cells for solar hydrogen production: current state of promising photoelectrodes, methods to improve their properties, and outlook, Energy Environ. Sci. 6 (2013) 347–370.

[2] C. Fàbrega, T. Andreu, F. Güell, J.D. Prades, S. Estradé, J.M. Rebled, et al., Effectiveness of nitrogen incorporation to enhance the photoelectrochemical activity of nanostructured TiO_2:NH_3 versus H_2-N_2 annealing., Nanotechnology. 22 (2011) 235403.

[3] C. Fàbrega, T. Andreu, A. Tarancón, C. Flox, A. Morata, L. Calvo-Barrio, et al., Optimization of surface charge transfer processes on rutile TiO2 nanorods photoanodes for water splitting, Int. J. Hydrogen Energy. 38 (2013) 2979–2985.

[4] D. Monllor-Satoca, M. Bärtsch, C. Fàbrega, A. Genç, S. Reinhard, T. Andreu, et al., What do you do, titanium? Insight into the role of titanium oxide as a water oxidation promoter in hematite-based photoanodes, Energy Environ. Sci. (2015).

[5] J. Su, X. Feng, J.D. Sloppy, L. Guo, C.A. Grimes, Vertically Aligned WO_3 Nanowire Arrays Grown Directly on Transparent Conducting Oxide Coated Glass: Synthesis and Photoelectrochemical Properties, Nano Lett. 11 (2010) 203–208.

[6] W. Kim, T. Tachikawa, D. Monllor-Satoca, H. Kim, T. Majima, W. Choi, Promoting water photooxidation on transparent WO_3 thin films using an alumina overlayer, Energy Environ. Sci. 6 (n.d.) 3732–3739.

[7] C. Santato, M. Ulmann, J. Augustynski, Enhanced Visible Light Conversion Efficiency Using Nanocrystalline WO_3 Films, Adv. Mater. 13 (2001) 511–514.

[8] J. Brillet, J.-H. Yum, M. Cornuz, T. Hisatomi, R. Solarska, J. Augustynski, et al., Highly efficient water splitting by a dual-absorber tandem cell, Nat. Photonics. 6 (2012) 824–828.

[9] Y. Park, K.J. McDonald, K.-S. Choi, Progress in bismuth vanadate photoanodes for use in solar water oxidation, Chem. Soc. Rev. 42 (2013) 2321–2337.

[10] T.W. Kim, K.-S. Choi, Nanoporous $BiVO_4$ photoanodes with dual-layer oxygen evolution catalysts for solar water splitting, Science (80-.). 343 (2014) 990–994.

[11] F.F. Abdi, L. Han, A.H.M. Smets, M. Zeman, B. Dam, R. van de Krol, Efficient solar water splitting by enhanced charge separation in a bismuth vanadate-silicon tandem photoelectrode., Nat. Commun. 4 (2013) 2195.

[12] F.F. Abdi, T.J. Savenije, M.M. May, B. Dam, R. van de Krol, The Origin of Slow Carrier Transport in $BiVO_4$ Thin Film Photoanodes: A Time-Resolved Microwave Conductivity Study, J. Phys. Chem. Lett. 4 (2013) 2752–2757.

[13] K. Sivula, F. Le Formal, M. Grätzel, WO_3–Fe_2O_3 Photoanodes for Water Splitting: A Host Scaffold, Guest Absorber Approach, Chem. Mater. 21 (2009) 2862–2867.

[14] J. Su, L. Guo, N. Bao, C.A. Grimes, Nanostructured WO_3/$BiVO_4$ Heterojunction Films for Efficient Photoelectrochemical Water Splitting, Nano Lett. 11 (2011) 1928–1933.

[15] X. Shi, I.Y. Choi, K. Zhang, J. Kwon, D.Y. Kim, J.K. Lee, et al., Efficient photoelectrochemical hydrogen production from bismuth vanadate-decorated tungsten trioxide helix nanostructures, Nat. Commun. 5 (2014) 4775.

[16] Z. Wang, G. Liu, C. Ding, Z. Chen, F. Zhang, J. Shi, et al., Synergetic Effect of Conjugated $Ni(OH)_2$ /IrO_2 Cocatalyst on Titanium-Doped Hematite Photoanode for Solar Water Splitting, J. Phys. Chem. C. 119 (2015) 19607–19612.

[17] G. Wang, Y. Ling, H. Wang, X. Yang, C. Wang, J.Z. Zhang, et al., Hydrogen-treated WO_3 nanoflakes show enhanced photostability, Energy Environ. Sci. 5 (2012) 6180–6187.

[18] J. Zhang, P. Zhang, T. Wang, J. Gong, Monoclinic WO_3 nanomultilayers with preferentially exposed (002) facets for photoelectrochemical water splitting, Nano Energy. 11 (2015) 189–195.

[19] C. Liu, N.P. Dasgupta, P. Yang, Semiconductor Nanowires for Artificial Photosynthesis, Chem. Mater. 26 (2014) 415–422.

[20] J.H. Kennedy, Photooxidation of Water at α-Fe_2O_3 Electrodes, J. Electrochem. Soc. 125 (1978) 709.

[21] S. Soedergren, A. Hagfeldt, J. Olsson, S.-E. Lindquist, Theoretical Models for the Action Spectrum and the Current-Voltage Characteristics of Microporous Semiconductor Films in Photoelectrochemical Cells, J. Phys. Chem. 98 (1994) 5552–5556.

[22] H. Wang, J. He, A. Hagfeldt, S. Lindquist, Photolelectrochemistry of Nanostructured WO_3 Thin Film Electrodes for Water Oxidation : Mechanism of Electron Transport, J. Phys. Chem. B. 104 (2000) 5686–5696.

[23] J. Navas, E. Guillén, R. Alcántara, C. Fernández-Lorenzo, J. Martín-Calleja, G. Oskam, et al., Direct Estimation of the Electron Diffusion Length in Dye-Sensitized Solar Cells, J. Phys. Chem. Lett. 2 (2011) 1045–1050.

[24] D. Monllor-Satoca, L. Borja, A. Rodes, R. Gómez, P. Salvador, Photoelectrochemical behavior of nanostructured WO_3 thin-film electrodes: The oxidation of formic acid., Chemphyschem. 7 (2006) 2540–51.

[25] R.A. Pala, A.J. Leenheer, M. Lichterman, H.A. Atwater, N.S. Lewis, Measurement of minority-carrier diffusion lengths using wedge-shaped semiconductor photoelectrodes, Energy Environ. Sci. 7 (2014) 3424–3430.

[26] C. Fàbrega, D. Monllor-Satoca, S. Ampudia, A. Parra, T. Andreu, J.R. Morante, Tuning the fermi level and the kinetics of surface states of TiO_2 nanorods by means of ammonia treatments, J. Phys. Chem. C. 117 (2013) 20517–20524.

[27] E. Comini, V. Guidi, C. Malagù, G. Martinelli, Z. Pan, G. Sberveglieri, et al., Electrical Properties of Tin Dioxide Two-Dimensional Nanostructures, J. Phys. Chem. B. 108 (2004) 1882–1887.

[28] K. Itoh, Thin Film Photoelectrochemistry: Iron Oxide, J. Electrochem. Soc. 131 (1984) 1266.

[29] H. Dotan, O. Kfir, E. Sharlin, O. Blank, M. Gross, I. Dumchin, et al., Resonant light trapping in ultrathin films for water splitting., Nat. Mater. 12 (2013) 158–64.

[30] A. Kay, I. Cesar, M. Gratzel, New Benchmark for Water Photooxidation by Nanostructured α-Fe_2O_3 Films, J. Am. Chem. Soc. 128 (2006) 15714–15721.

[31] Y. Qiu, S.-F. Leung, Q. Zhang, B. Hua, Q. Lin, Z. Wei, et al., Efficient photoelectrochemical water splitting with ultrathin films of hematite on three-dimensional nanophotonic structures., Nano Lett. 14 (2014) 2123–9.

[32] J.M. Spurgeon, J.M. Velazquez, M.T. McDowell, Improving O_2 production of WO_3 photoanodes with IrO_2 in acidic aqueous electrolyte., Phys. Chem. Chem. Phys. 16 (2014) 3623–31.

[33] C.R. Lhermitte, J. Garret Verwer, B.M. Bartlett, Improving the stability and selectivity for the oxygen-evolution reaction on semiconducting WO_3 photoelectrodes with a solid-state FeOOH catalyst, J. Mater. Chem. A. (2016).

[34] Q. Mi, A. Zhanaidarova, B.S. Brunschwig, H.B. Gray, N.S. Lewis, A quantitative assessment of the competition between water and anion oxidation at WO_3 photoanodes in acidic aqueous electrolytes, Energy Environ. Sci. 5 (2012) 5694.